University of California

Los Angeles

Microstructural Feature-based Processing and Analysis of Diffusion Tensor MRI

A dissertation submitted in partial satisfaction

of the requirements for the degree

Doctor of Philosophy in Computer Science

by

Jin Kyu Gahm

2014

Abstract of the Dissertation

Microstructural Feature-based Processing and Analysis of Diffusion Tensor MRI

by

Jin Kyu Gahm

Doctor of Philosophy in Computer Science

University of California, Los Angeles, 2014

Professor Daniel B. Ennis, Co-chair

Professor Demetri Terzopoulos, Co-chair

Tensors increasingly arise in a variety of medical imaging and image processing contexts. Diffusion tensor magnetic resonance imaging (DT-MRI) measures the self-diffusion rate of water molecules within small volumes of biological tissues to characterize their microstructural features. The diffusion tensor can be decomposed into shape and orientation components, and the shape components are intuitively and saliently characterized by tensor invariants. Hence the invariant and orientation information implies the microstructural features of tissues. The mathematical framework that freely builds tensors from tensor invariants has been recently established, and allowed for developing novel approaches for processing and analysis of diffusion tensor fields. New tensor interpolation methods are devised that linearly interpolate each of tensor invariants and orientations to preserve cardiac microstructural features. The uniform tensor invariant set is proposed that linearly characterizes tensor shape, and provides more accurate tensor field interpolation and analysis of cardiac diffusion tensor fields. A microstructural feature-based tensor distance is also defined by a linear combination of tensor invariant and orientation distances, and applied to graph-based segmentation of cardiac diffusion tensor fields. Finally, the effects of noise in DT-MRI

are evaluated on tensor invariants characterizing tensor shape over the complete space of tensor shape. In addition, a new framework is developed for determining the distribution of the likely true values of tensor invariants given their noisy measures.

The dissertation of Jin Kyu Gahm is approved.

Alan Garfinkel

Alan L. Yuille

Douglas S. Parker

Demetri Terzopoulos, Committee Co-chair

Daniel B. Ennis, Committee Co-chair

University of California, Los Angeles

2014

This dissertation is dedicated

to my parents

for their love, endless support

and encouragement.

Table of Contents

List of Figures

List of Tables

Acknowledgments

My profound thanks to my co-advisor Daniel Ennis for his support and encouragement over the past five years. He has been a great mentor, colleague, and friend. His exceptional guidance has made this a truly rewarding experience. In addition, I would like to express my immense gratitude to my other co-advisor Demetri Terzopoulos for his advice and support.

I would like to thank the other doctoral committee members: Stott Parker, Alan Garfinkel and Alan Yuille for their support. I am also grateful to my collaborators: William Klug, Nick Wisniewski, Shankarjee Krishnamoorthi, Gordon Kindlmann, and all my lab members.

This dissertation work was supported, in part, by research support from the Department of Radiological Sciences at UCLA.

Vita

2000	B.S. (Computer Science and Engineering), Seoul National University, Korea.
2002	Teaching Assistant, Department of Computer Science, Rensselaer Polytechnic Institute, Troy, NY.
2002–2003	Research Assistant, Department of Computer Science, Rensselaer Polytechnic Institute, Troy, NY.
2003	M.S. (Computer Science), Rensselaer Polytechnic Institute, Troy, NY.
2003–2007	Software/Hardware Engineer, Samsung Electronics Co., Korea.
2009–2014	Graduate Student Researcher, Department of Radiological Sciences, University of California, Los Angeles, CA.

Publications

Journal

Gahm JK, Kindlmann G, Ennis DB. The effects of noise over the complete space of diffusion tensor shape. Medical Image Analysis 18, pp. 197–210, 2014.

Kung GL, Ouadah S, Hsieh YC, Gahm JK, Garfinkel A, Chen PS, Ennis DB. Myocardial microstructural remodeling in pacing induced heart failure measured by diffusion tensor MRI. Journal of Magnetic Resonance Imaging. {In preparation}.

Kung GL, Vaseghi M, Gahm JK, Shevtsov J, Garfinkel A, Shivkumar K, Ennis DB. Microstructural border zone remodeling in the post-infarct porcine heart measured by diffusion tensor MRI and T1-weighted late gadolinium enhanced MRI. Journal of Magnetic Resonance Imaging. {In preparation}.

Conference Paper

Kettnaker V, Gahm JK. Closed-loop person tracking and detection. Computer and Robot Vision, 2004. First Canadian Conference on, pp. 315–320, 2004.

Gahm JK, Wisniewski N, Kindlmann G, Kung GL, Klug WS, Garfinkel A, Ennis DB. Linear invariant tensor interpolation applied to cardiac diffusion tensor MRI. Medical Image Computing and Computer-Assisted Intervention (MICCAI) 2012, Part II. LNCS 7511, pp. 494–501, 2012.

Gahm JK, Kung GL, Ennis DB. Weighted component-based tensor distance applied to graph-based segmentation of cardiac DT-MRI. Biomedical Imaging (ISBI), 2013 IEEE 10th International Symposium on, pp. 504–507, 2013.

Gahm JK, Ennis DB. Dyadic tensor-based interpolation of tensor orientation: application to cardiac DT-MRI. Statistical Atlases and Computational Models of the Heart (STACOM), MICCAI Workshop 2013, LNCS 8330, pp. 135–142, 2014.

Gahm JK, Ennis DB. Uniform tensor invariant set and the application in cardiac DT-MRI. Medical Image Computing and Computer-Assisted Intervention (MICCAI) 2014. {Submitted}.

Conference Abstract

Gahm JK, Wisniewski N, Klug WS, Garfinkel A, Ennis DB. Statistical comparison of DT-MRI interpolation methods using cardiac DT-MRI data. International Society for Magnetic Resonance in Medicine (ISMRM) 19th Annual Meeting, Montreal, Canada, p. 3894, May 2011.

Kung GL, Ajijola O, Ramirez RJ, Gahm JK, Zhou W, Wisniewski N, Mahajan A, Garfinkel A, Shivkumar K, Ennis DB. Microstructural remodeling in the post-infarct porcine heart measured by diffusion tensor MRI and T1-weighted late gadolinium enhancement MRI. 15th Annual Society for Cardiovascular Magnetic Resonance (SCMR) Scientific Sessions, Orlando, FL, February 2012.

Kung GL, Gahm JK, Garfinkel A, Chen PS, Ennis DB. Microstructural remodeling in pacing induced heart failure measured by diffusion tensor MRI. Biomedical Engineering Society (BMES) Annual Meeting, Atlanta, GA, October 2012.

Kung GL, Vaseghi M, Gahm JK, Shevtsov J, Garfinkel A, Shivkumar K, Ennis DB. Microstructural border zone remodling in the post-infarct porcine heart measured by diffusion tensor MRI and late gadolinium enhancement MRI. Cardiac Physiome Society Annual Workshop, San Diego, CA, October 2012.

Kung GL, Ajijola O, Tung R, Vaseghi M, Gahm JK, Zhou W, Mahajan A, Garfinkel A, Shivkumar K, Ennis DB. Microstructural remodling in the porcine infarct border zone measured by diffusion tensor and late gadolinium enhancement MRI. American Heart Association (AHA) Scientific Sessions, Los Angeles, CA, November 2012.

CHAPTER 1

Introduction

Tensors increasingly arise in a variety of medical imaging and image processing contexts. Second-order tensors in three-dimensional space, in particular, are useful quantities because they describe linear transformations between vectors in the space. The central focus of the work described herein is the processing and analysis of diffusion tensor magnetic resonance imaging (DT-MRI) data, which measures the self-diffusion tensor of water molecules within small volumes of soft biological tissues [Basser et al., 1994a]. Attributes of DT-MRI are now widely used to characterize the local microstructural environment including diffusive shape and microstructural orientation within the brain [Basser and Pierpaoli, 1996], heart [Scollan et al., 1998, Hsu et al., 1998, Kung et al., 2011], and other tissues.

Diffusion tensors are represented as 3×3 symmetric positive definite matrices that can be decomposed into a system of three eigenvectors and three positive eigenvalues. More generally, diffusion tensors can be decomposed into independent shape and orientation components. The shape components describe the overall and relative sizes of the principal axes (rates of diffusion) and are, in general, independent of the chosen coordinate system. The orientation components describe the relationship between the principal axes and a local coordinate system. Most commonly, the shape components are characterized by the eigenvalues and the orientation components are described by the eigenvectors.

The individual eigenvalues, however, fail to isolate the salient geometric features of tensor shape. Tensor invariants are the preferred means for characterizing

tensor shape and are considered to report important, if not intuitive, properties of the underlying diffusive process [Basser et al., 1994b]. Tensor invariants can be used to categorize tensor shape attributes into three independent components: the magnitude-of-isotropy (tensor trace, determinant or norm), magnitude-of-anisotropy (fractional or relative anisotropy) and kind-of-anisotropy (tensor mode or skewness) [Ennis and Kindlmann, 2006, Kindlmann et al., 2007a]. DT-MRI data have been used extensively to evaluate microstructural organization and remodeling in health and disease by investigating the magnitudes or changes in tensor invariants including tensor trace, fractional anisotropy (FA) and mode [Sotak, 2002, Thomalla et al., 2004, Jolapara et al., 2009].

Tensor orientation is commonly represented by a rotation matrix consisting of the three eigenvectors. Other representations include a unit quaternion and Euler angles – common alternatives to the rotation matrix in computer graphics [Shoemake, 1985]. In cardiac applications the primary eigenvector corresponds to the direction of fastest diffusion, which has been shown to align with the long axis of the myocytes that comprise the heart [Scollan et al., 1998, Hsu et al., 1998, Kung et al., 2011]. The secondary and tertiary eigenvectors correspond to the crossfiber-within-sheet direction and the sheet normal direction, respectively [Kung et al., 2011].

1.1 Motivation

The diffusion tensor shape and orientation information are important components of computational models of cardiac mechanics and electrophysiology (EP) [Krishnamoorthi et al., 2013]. EP models require millions of closely spaced nodes that do not necessarily lie at lattice points. DT-MRI measurements, however, are on a lattice and typically number $\ll 1e6$ so interpolation of the diffusion tensors is needed. The conventional methods of tensor interpolation are mostly based on

the Riemannian space formed by symmetric positive definite tensors [Batchelor et al., 2005, Fletcher and Joshi, 2007, Lenglet et al., 2006, Pennec et al., 2006, Arsigny et al., 2006]. The tensor-based Riemannian approaches maintain the tensor determinant but underestimate tensor trace and FA [Kindlmann et al., 2007b]. The Riemannian space-based methods are mathematically convenient but, as will be shown, do not preserve microstructural features.

The research in this dissertation is motivated by the problem of the most widely used Riemannian approaches that were developed on the tensor level without specific regard for tissue microstructure. We suggest an approach for tensor field processing on the level of the shape and orientation components of the tensor that characterize microstructural features. The microstructural feature-based interpolation is accomplished by directly interpolating each component of tensor shape (tensor invariants) and orientation (eigenvectors). To do so, we developed the mathematics for converting tensor invariants into eigenvalues [Gahm et al., 2014]. This allows for the separate interpolation of tensor invariants and eigenvectors and subsequent recapitulation of the tensor from the interpolated components.

The mathematical framework that freely converts between tensor invariants and eigenvalues are also used to develop novel approaches for the analysis of diffusion tensor fields. The noise immunity of tensor invariants has previously been investigated, by simulation, mostly under an assumption of cylindrically symmetric anisotropy [Pierpaoli and Basser, 1996, Jones, 2004, Kingsley and Monahan, 2005]. This assumption is convenient, but not acceptable for all applications. The mathematical conversion between tensor invariants and eigenvalues, therefore, enables tensor invariant-based evaluation of the effects of noise over the complete space of tensor shape.

These microstructural feature-based tensor processing and analysis tasks require an appropriate tensor invariant set that characterizes features of microstruc-

tural shape. One may spontaneously choose a set including FA and mode because they are widely used in the literature. We observe, however, that FA and mode do not characterize their tensor components in a linear manner, that is, their equally spaced values produce non-equal distances between the eigenvalues. Motivated by this observation, we develop a new tensor invariant set that linearly characterizes tensor shape. Such a tensor invariant set that logically quantifies a change in tensor shape allows for more accurate microstructural feature-based tensor processing and analysis.

1.2 Overview

The overall objective of this dissertation was to develop mathematically unambiguous and computationally efficient methods for processing, interpolating and analyzing diffusion tensor fields that preserve features of microstructural shape and orientation. This was achieved by tensor field processing directly on each component of tensor shape and orientation (tensor invariants and eigenvectors), and subsequent recapitulation of the tensor from the tensor components for further tensor-based processing and analysis.

Chapter 2 provides a mathematical introduction to establish terminology commonly used throughout the dissertation including the basic mathematics of diffusion tensors and descriptions of tensor shape and orientation. This chapter also introduces the mathematics for conversion between the tensor shape descriptions (eigenvalues and invariants) that is important because work throughout the dissertation is based on the mathematical framework for tensor decomposition and reconstruction using tensor invariants.

Chapter 3 describes a tensor shape interpolation method that linearly interpolates components of tensor shape (tensor invariants). The tensor invariant-based method is compared to the conventional tensor-based methods including the Rie-

mannian approaches using experimentally measured cardiac DT-RMI data. Our method is shown to better recover the features of cardiac microstructural shape at substantially reduced computational cost.

Chapter 4 describes a tensor orientation interpolation method that interpolates between the dyadic tensors of eigenvectors. The dyadic tensor-based method that sidesteps the eigenvector sign ambiguity problem is compared to the conventional tensor-based methods for recovery of the cardiac microstructural orientation. Our method has significantly less bias for recovery of the secondary and tertiary eigenvector, which is especially important for interpolating myolaminar sheet orientation in the heart.

Chapter 5 defines a new weighted component-based tensor distance that linearly combines tensor shape (three tensor invariants) and orientation distances. Moreover the weighted component-based tensor distance allows users to easily adjust relative contributions of the distance components toward an optimal single distance for a particular application. It is applied to graph-based multi-label segmentation of DT-MRI data from infarcted hearts, and compared to other conventional metrics. The segmentation results using each metric are presented to show that the weighted component-based tensor distance is both simple and more accurate.

Chapter 6 describes the fundamental work that evaluates by simulation the effects of noise on characterizing tensor shape over the complete space of tensor shape for different DT-MRI encoding schemes. Previous work has only examined the impact of noise over a narrow range of tensor shape. A new framework is also defined that determines the distribution of the true values of the observed tensor invariants given their noisy measures, which provides guidance about the confidence the observer should have in the measured tensor invariants. The statistics of tensor invariant estimates over the complete space of tensor shape are presented to demonstrate how the noise sensitivity of tensor invariants varies across the space

of tensor shape as well as how the DT-MRI acquisition protocol impacts measures of tensor invariants.

Chapter 7 presents a new tensor invariant set consisting of trace, relative anisotropy (RA) and angular mode (the arccos of mode), termed *uniform tensor invariant set*, that more logically (linearly) characterizes the complete space of tensor shape. Linearity is mathematically proven by showing that evenly spaced values of each tensor invariant in the set produce uniform distances between the eigenvalues for each step exclusively. FA and mode fail to produce equal distances between the eigenvalues for each step. The logical property of the uniform tensor invariant set is demonstrated by comparison of the uniform tensor invariants to FA and mode for tensor field interpolation and analysis of experimentally measured cardiac diffusion tensor fields.

Finally Chapter 8 concludes the dissertation by summarizing the important aspects of the work and discussing potential future work.

1.3 Contributions

The primary contributions of this dissertation are summarized:

- Development of tensor invariant-based interpolation of tensor shape (Chapters 3 and 7) [Gahm et al., 2012, Gahm and Ennis, 2014b]. Previous tensor-based interpolation methods were mathematically convenient, but did not preserve important microstructural features.

- Development of dyadic tensor-based interpolation of tensor orientation (Chapter 4) [Gahm and Ennis, 2014a]. This is the first use of the dyadic tensors of eigenvectors to resolve the eigenvector sign ambiguity problem.

- Development of a microstructural feature-based measurement of tensor distance with different weights (Chapter 5) [Gahm et al., 2013]. Previous

tensor-based metrics provided a single overall tensor distance with unknown, fixed contributions of the microstructural features.

- Evaluation of the effects of noise on characterizing tensor shape over the *complete* space of tensor shape (Chapter 6) [Gahm et al., 2014]. The effects of noise were previously investigated only over a *narrow* range of tensor shape.

- Development of a new tensor invariant set that linearly characterizes tensor shape (Chapter 7) [Gahm and Ennis, 2014b]. Though widely used evenly spaced values of FA and mode failed to produce equal distances between the eigenvalues for each step.

CHAPTER 2

Background

This chapter describes mathematical background commonly used for the research in this dissertation. Each subsequent chapter has its own introduction and theory sections that provide considerably more background that is specific to the research described within the chapter.

2.1 Mathematical Background

2.1.1 Tensor Algebra Basics

Tensors, in general, are geometrical objects that describe linear transformations between scalars, vectors, and other tensors. A second-order tensor represents a linear transformation between vector spaces, where the vector space in this work is the three-dimensional Euclidean space $\mathbb{R}^3$. That is, a second-order tensor $\mathbf{D}$ maps an input vector $\mathbf{u}$ to another vector $\mathbf{v} = \mathbf{D}\mathbf{u}$. This mapping is *linear* in the sense that:

$$\begin{aligned} &\mathbf{D}(\mathbf{u}+\mathbf{v}) = \mathbf{D}\mathbf{u} + \mathbf{D}\mathbf{v},\ \forall \mathbf{u}, \mathbf{v} \in \mathbb{R}^3\ , \\ &\mathbf{D}(\alpha\mathbf{u}) = \alpha\mathbf{D}\mathbf{u},\ \forall \alpha \in \mathbb{R}, \mathbf{u} \in \mathbb{R}^3\ . \end{aligned} \tag{2.1}$$

Examples of such second-order tensors include projections, rotations, and reflections. All tensors in this work will be second-order.

A tensor $\mathbf{D}$ is called *symmetric* if $\mathbf{D} = \mathbf{D}^T$, or *skew-symmetric* if $\mathbf{D} = -\mathbf{D}^T$. A non-invertible tensor is called *singular*. A tensor $\mathbf{D}$ is said to be *positive definite*

if $\mathbf{v} \cdot \mathbf{D}\mathbf{v}$ is positive, or *positive semi-definite* if $\mathbf{v} \cdot \mathbf{D}\mathbf{v}$ is non-negative, for any non-zero vector $\mathbf{v} \in \mathbb{R}^3$.

The *dyadic product* (tensor product) of two vectors $\mathbf{u}$ and $\mathbf{v}$ is the second-order, rank-one tensor $\mathbf{u} \otimes \mathbf{v}$, termed a *dyad*, and defined by:

$$(\mathbf{u} \otimes \mathbf{v})\mathbf{w} = (\mathbf{v} \cdot \mathbf{w})\mathbf{u}, \ \forall \mathbf{w} \in \mathbb{R}^3 \ . \tag{2.2}$$

2.1.2 Matrix Representations

A vector or tensor has a unique matrix representation in an ordered basis. Orthonormal bases consist of vectors that are mutually orthogonal with unit length. Tensors represented in orthonormal bases are called *Cartesian*, and only Cartesian tensors are used in this work.

Given a ordered orthonormal basis $\mathcal{B} = \{\mathbf{b}_1, \mathbf{b}_2, \mathbf{b}_3\}$ for $\mathbb{R}^3$, a vector $\mathbf{v}$ can be represented in a matrix form:

$$[\mathbf{v}]_{\mathcal{B}} = \begin{bmatrix} v_1 \\ v_2 \\ v_3 \end{bmatrix}, \ v_i = \mathbf{b}_i \cdot \mathbf{v} \ . \tag{2.3}$$

Then any vector v can be uniquely expressed as a linear combination:

$$\mathbf{v} = \sum_{i=1}^{3} v_i \mathbf{b}_i = \sum_{i=1}^{3} (\mathbf{b}_i \cdot \mathbf{v})\mathbf{b}_i \ , \tag{2.4}$$

A tensor can be represented in a matrix form:

$$[\mathbf{D}]_{\mathcal{B}} = \begin{bmatrix} D_{11} & D_{12} & D_{13} \\ D_{21} & D_{22} & D_{23} \\ D_{31} & D_{32} & D_{33} \end{bmatrix}, \ D_{ij} = \mathbf{b}_i \cdot \mathbf{D}\mathbf{b}_j \ . \tag{2.5}$$

We call $[\mathbf{D}]$ the matrix representation in an arbitrary basis. The matrix representation of a dyadic product $\mathbf{u} \otimes \mathbf{v}$ is the *outer product* of the matrix representations

of $\mathbf{u}$ and $\mathbf{v}$:

$$[\mathbf{u} \otimes \mathbf{v}]_{\mathcal{B}} = [\mathbf{u}]_{\mathcal{B}}[\mathbf{v}]_{\mathcal{B}}^{T} = \begin{bmatrix} u_1v_1 & u_1v_2 & u_1v_3 \\ u_2v_1 & u_2v_2 & u_2v_3 \\ u_3v_1 & u_3v_3 & u_3v_3 \end{bmatrix} . \tag{2.6}$$

In particular, the nine dyadic products of the basis vectors, $\{\mathbf{b}_i \otimes \mathbf{b}_j\}$, form a *basis* for the set of all second-order tensors on $\mathbb{R}^3$. Any tensor $\mathbf{D}$ can be uniquely represented as a linear combination:

$$\mathbf{D} = \sum_{j=1}^{3}\sum_{i=1}^{3} D_{ij}\mathbf{b}_i \otimes \mathbf{b}_j = \sum_{j=1}^{3}\sum_{i=1}^{3}(\mathbf{b}_i \cdot \mathbf{D}\mathbf{b}_j)\mathbf{b}_i \otimes \mathbf{b}_j \ . \tag{2.7}$$

In the DT-MRI literature, a diffusion tensor is commonly represented by a *symmetric positive-definite* matrix in the coordinate frame made by the MRI scanner. This coordinate frame is called the *laboratory frame*, which will be denoted by $\mathcal{L}$:

$$[\mathbf{D}]_{\mathcal{L}} = \begin{bmatrix} D_{xx} & D_{xy} & D_{xz} \\ D_{xy} & D_{yy} & D_{yz} \\ D_{xz} & D_{yz} & D_{zz} \end{bmatrix} . \tag{2.8}$$

There are six degrees of freedom for such symmetric tensors.

2.1.3 Eigenvalues and Eigenvectors

A unit vector $\mathbf{e}$ is an *eigenvector* of a tensor $\mathbf{D}$ satisfying the linear equation:

$$\mathbf{D}\mathbf{e} = \lambda\mathbf{e} \ \Leftrightarrow \ (\lambda\mathbf{I} - \mathbf{D})\mathbf{e} = 0 \ , \tag{2.9}$$

where a scalar λ is called the *eigenvalue* corresponding to $\mathbf{e}$. Since the tensor $\lambda\mathbf{I} - \mathbf{D}$ is singular, the eigenvalues are the roots of the *characteristic (cubic) polynomial*:

$$p(\lambda) = \det(\lambda\mathbf{I} - \mathbf{D}) \ . \tag{2.10}$$

The eigenvectors $\mathbf{e}$ associated with each eigenvalue λ_i are obtained by solving Eq. 2.9.

When $\mathbf{D}$ is symmetric, all three eigenvalues are real (positive if $\mathbf{D}$ is positive definite), and all the associated eigenvectors are also real and mutually orthogonal. Then there exists a *right-handed*, *orthonormal* basis consisting solely of eigenvectors of $\mathbf{D}$, $\mathcal{E} = \{\mathbf{e}_1, \mathbf{e}_2, \mathbf{e}_3\}$, called the *principal frame*. The matrix representation of $\mathbf{D}$ in the principal frame is represented as a diagonal matrix of eigenvalues from Eq. 2.5:

$$([\mathbf{D}]_{\mathcal{E}})_{ij} = \mathbf{e}_i \cdot \mathbf{D}\mathbf{e}_j = \mathbf{e}_i \cdot \lambda_j \mathbf{e}_j \ ,$$

which yields

$$[\mathbf{D}]_{\mathcal{E}} = \Lambda = \begin{bmatrix} \lambda_1 & 0 & 0 \\ 0 & \lambda_2 & 0 \\ 0 & 0 & \lambda_3 \end{bmatrix} \ , \tag{2.11}$$

where the eigenvalues are typically sorted in decreasing order ($\lambda_1 \geq \lambda_2 \geq \lambda_3$). From Eq. 2.12, the *spectral decomposition* (dyadic representation) of $\mathbf{D}$ is:

$$\mathbf{D} = \sum_{i=1}^{3} \lambda_i \mathbf{e}_i \otimes \mathbf{e}_i \ . \tag{2.12}$$

A diffusion tensor represented in the laboratory frame $[\mathbf{D}]_{\mathcal{L}}$ in Eq. 2.8 can be factorized as:

$$\begin{aligned} [\mathbf{D}]_{\mathcal{L}} &= \mathbf{R}\Lambda\mathbf{R}^T \\ \mathbf{R} &= \begin{bmatrix} [\mathbf{e}_1]_{\mathcal{L}} & [\mathbf{e}_2]_{\mathcal{L}} & [\mathbf{e}_3]_{\mathcal{L}} \end{bmatrix} \ , \end{aligned} \tag{2.13}$$

where $\mathbf{R}$ is a rotation matrix in which each column is an eigenvector represented in the laboratory frame.

2.2 Tensor Shape

A diffusion tensor $\mathbf{D}$ can be decomposed into independent tensor *shape* and *orientation* components. The shape components are commonly characterized by the three eigenvalues λ_i, and the orientation components by the three eigenvectors $\mathbf{e}_i$

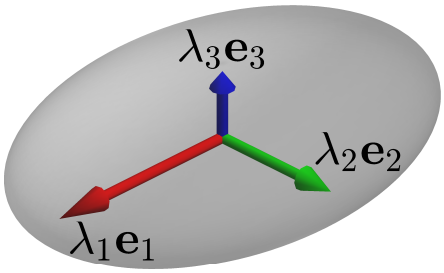

Figure 2.1: An ellipsoid that visually represents a diffusion tensor. The axes are aligned with the eigenvectors and scaled by the eigenvalues.

of $\mathbf{D}$. Therefore, the shape components have three degrees of freedom of $\mathbf{D}$ (six degrees of freedom), spanned by changes of λ_i with fixed $\mathbf{e}_i$, and the orientation components have another three degrees of freedom of $\mathbf{D}$, spanned by changes of $\mathbf{e}_i$ with fixed λ_i. The shape and orientation components characterized by the eigenvalues and eigenvectors can be graphically represented as an *ellipsoid* in the principal frame of $\mathbf{D}$, where its axes are aligned with the eigenvectors and scaled by the eigenvalues (Fig. 2.1).

2.2.1 Tensor Invariants

Each eigenvalue characterizes the length of the corresponding principal axis (eigenvector). However, individual eigenvalues fail to isolate more salient geometric shape properties such as the overall size and relative sizes of the principal axes. Tensor *invariants* are the preferred means to characterize such salient properties of the underlying diffusive process in DT-MRI [Basser et al., 1994b, Ennis and Kindlmann, 2006, Kindlmann et al., 2007a]. The term "invariant" implies that their value is unchanged by a change to the choice of basis (coordinate system) for the matrix representation of the tensor.

Tensor invariants are categorized into three independent components of tensor shape: the magnitude of isotropy, magnitude of anisotropy and kind of anisotropy. The magnitude of isotropy describes some aspect of the overall size and is char-

acterized, for example, by tensor trace (three times mean diffusivity), norm or determinant. The magnitude of anisotropy quantifies the extent to which the diffusion rates are directionally dependent, and can be characterized by fractional anisotropy (FA) or relative anisotropy (RA) [Basser, 1995]. The kind of anisotropy describes another property of tensor anisotropy from planar anisotropy, to orthotropy, to linear anisotropy, and can be characterized by tensor *mode* [Criscione et al., 2000] or skewness.

2.2.2 Orthogonal Tensor Invariant Sets

The two sets of orthogonal tensor invariants have been described previously by [Ennis and Kindlmann, 2006]. The term "orthogonal tensor invariant set" indicates that all permutations of tensorial contraction of the gradients of each invariant J_i within a set are zero:

$$\frac{\partial J_i}{\partial \mathbf{D}} : \frac{\partial J_j}{\partial \mathbf{D}} = 0, \ (i \neq j) \ . \tag{2.14}$$

Each orthogonal tensor invariant includes a measure characterizing one of the three degrees of freedom of tensor shape, the magnitude of isotropy (K_1 or R_1), the magnitude of anisotropy (K_2 or R_2), and the mode of anisotropy ($K_3 = R_3$). The $J_i = K_i$ set of orthogonal tensor invariants includes the tensor trace (K_1), RA(K_2), mode (K_3), and are defined for a tensor $\mathbf{D}$ as follows:

$$\begin{aligned} K_1 &= \mathrm{tr}\mathbf{D} \\ K_2 &= \mathrm{norm}\widetilde{\mathbf{D}} \\ K_3 &= \mathrm{mode}\widetilde{\mathbf{D}} = \frac{3\sqrt{6}\det\widetilde{\mathbf{D}}}{\left(\mathrm{norm}\widetilde{\mathbf{D}}\right)^3} \ , \end{aligned} \tag{2.15}$$

where tr is the tensor trace, norm is the tensor Frobenius norm, det is the tensor determinant, and deviatoric $\widetilde{\mathbf{D}} = \mathbf{D} - \frac{1}{3}\mathrm{tr}\mathbf{D}$.

The $J_i = R_i$ set of orthogonal tensor invariants includes the tensor norm (R_1),

FA (R_2), and mode($R_3 = K_3$), and are defined as follows:

$$\begin{aligned} R_1 &= \text{norm}\mathbf{D} \\ R_2 &= \sqrt{\frac{3}{2}}\frac{\text{norm}\widetilde{\mathbf{D}}}{\text{norm}\mathbf{D}} \\ R_3 &= K_3 \ . \end{aligned} \tag{2.16}$$

One advantage of orthogonal tensor invariants is that they characterize independent components of tensor shape. Orthogonality eliminates the mathematical correlation between the invariants, which implies statistical independence.

2.2.3 Non-orthogonal Invariant Set

Despite the advantage of using sets of orthogonal invariants (K_i or R_i), there is a tremendous volume of literature that analyzes DT-MRI data by evaluating the tensor trace (K_1) and FA (R_2), which has given rise to a body of knowledge and expectation about the values of these invariants and how they are altered by disease [Sotak, 2002, Thomalla et al., 2004, Jolapara et al., 2009]. Note, however, that K_1 is not orthogonal to R_2 (see [Ennis and Kindlmann, 2006]). Furthermore, these two degrees of freedom are not sufficient to completely describe tensor shape, and therefore tensor mode ($K_3 = R_3$) is also needed. Such a non-orthogonal, but popular invariant set $\{K_1, R_2, R_3\}$ is also used to fully characterize tensor shape in this work.

Note that the non-orthogonal invariant set including R_2 and R_3 is chosen due to their widespread use in the literature, but R_2 and R_3 are inappropriate for characterizing their components of tensor shape in a linear manner. It is desirable that tensor invariants and their corresponding tensor components have a linear relationship. This topic is more completely addressed in Chapter 7.

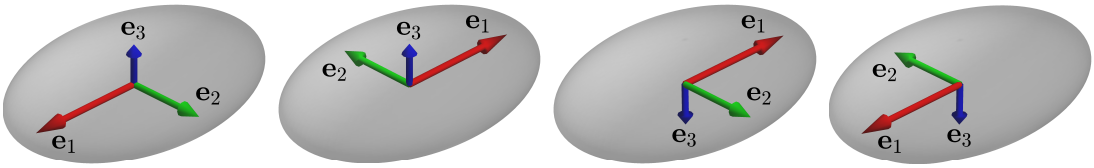

Figure 2.2: Four different descriptions of tensor orientation by changing the sign of each eigenvector preserving the right hand rule.

2.3 Tensor Orientation

Tensor orientation describes a rotation between the principal frame and the laboratory frame. Hence tensor orientation is commonly represented by the rotation matrix $\mathbf{R} \in \mathrm{SO}(3)$ consisting of three eigenvectors in the laboratory frame (Eq. 2.13). Tensor orientation can also be represented by a unit quaternion or Euler angles.

The sign of an eigenvector $\mathbf{e}_i$ is not unique, in general, because both $\mathbf{e}_i$ and $-\mathbf{e}_i$ satisfy the eigenvalue equation given in Eq. 2.9. The eigenvector sign ambiguity implies that tensor orientation cannot be uniquely described. There are four possibilities for a rotation matrix $\mathbf{R}$ preserving the SO(3) group ($\det \mathbf{R} = +1$):

$$\mathbf{R}_i = \mathbf{R}\mathbf{P}_i \ , \tag{2.17}$$

where $\mathbf{P}_i$ is a diagonal matrix of p_j such that $p_j = \pm 1$ and $p_1 p_2 p_3 = 1$. These can be considered as different bases preserving the right hand rule in the principal frame from Eq. 2.11 (Fig. 2.2).

2.4 Tensor Shape from Invariant Sets

We recently developed the mathematics that permits a tensor to be recapitulated from its shape and orientation components. In particular, if the eigenvalues (λ_i) and column eigenvectors ($\mathbf{e}_i$) are known, then the matrix expression for tensor $\mathbf{D}$ in the laboratory frame ($[\mathbf{D}]_{\mathcal{L}}$) can be obtained from Eq. 2.8. In order to recapitulate

a tensor from its tensor invariants and orientation information, a transformation between the tensor invariants and the eigenvalues must be formulated.

The eigenvalues of tensor $\mathbf{D}$ are found by solving the characteristic equation $p(\lambda) = 0$ in Eq. 2.10, which yields a simple cubic polynomial equation:

$$\lambda^3 + a\lambda^2 + b\lambda + c = 0 \ . \tag{2.18}$$

A closed-form solution for the eigenvalues can be formulated [Press, 2002]:

$$\begin{aligned} \lambda_1 &= \frac{a}{3} + 2\sqrt{Q}\cos\left(\frac{\Theta}{3}\right) \\ \lambda_2 &= \frac{a}{3} + 2\sqrt{Q}\cos\left(\frac{\Theta - 2\pi}{3}\right) \\ \lambda_3 &= \frac{a}{3} + 2\sqrt{Q}\cos\left(\frac{\Theta + 2\pi}{3}\right) \ , \end{aligned} \tag{2.19}$$

where

$$\begin{aligned} P &= \frac{2a^3 - 9ab + 27c}{54} \\ Q &= \frac{a^2 - 3b}{9} \\ \Theta &= \arccos\left(\frac{P}{\sqrt{Q^3}}\right) \ . \end{aligned} \tag{2.20}$$

By identifying the relationship between $\{P, Q, \Theta\}$ (or $\{a, b, c\}$) and the orthogonal tensor invariant set $\{K_i\}$, the expressions for the eigenvalues from the invariants were derived as [Gahm et al., 2014]:

$$\begin{aligned} \lambda_1 &= \tfrac{1}{3}K_1 + \sqrt{\tfrac{2}{3}}K_2\cos\left(\frac{\arccos\left(K_3\right)}{3}\right) \\ \lambda_2 &= \tfrac{1}{3}K_1 + \sqrt{\tfrac{2}{3}}K_2\cos\left(\frac{\arccos\left(K_3\right) - 2\pi}{3}\right) \\ \lambda_3 &= \tfrac{1}{3}K_1 + \sqrt{\tfrac{2}{3}}K_2\cos\left(\frac{\arccos\left(K_3\right) + 2\pi}{3}\right) \ . \end{aligned} \tag{2.21}$$

A similar result was first shown by [Criscione et al., 2000] and [Hasan et al., 2001].

Alternately, the expressions for the eigenvalues from the orthogonal invariant

set $\{R_i\}$ were given as [Gahm et al., 2014]:

$$\begin{aligned}
\lambda_1 &= \tfrac{1}{3}R_1\sqrt{3-2R_2^2} + \tfrac{2}{3}R_1R_2\cos\left(\frac{\arccos\left(R_3\right)}{3}\right) \\
\lambda_2 &= \tfrac{1}{3}R_1\sqrt{3-2R_2^2} + \tfrac{2}{3}R_1R_2\cos\left(\frac{\arccos\left(R_3\right)-2\pi}{3}\right) \\
\lambda_3 &= \tfrac{1}{3}R_1\sqrt{3-2R_2^2} + \tfrac{2}{3}R_1R_2\cos\left(\frac{\arccos\left(R_3\right)+2\pi}{3}\right) \ .
\end{aligned} \tag{2.22}$$

Finally, the expression for the eigenvalues from the non-orthogonal tensor invariant set $\{K_1, R_2, R_3\}$ were also given as [Gahm et al., 2014]:

$$\begin{aligned}
\lambda_1 &= \tfrac{1}{3}K_1 + \frac{2K_1R_2}{3\sqrt{3-2R_2^2}}\cos\left(\frac{\arccos\left(R_3\right)}{3}\right) \\
\lambda_2 &= \tfrac{1}{3}K_1 + \frac{2K_1R_2}{3\sqrt{3-2R_2^2}}\cos\left(\frac{\arccos\left(R_3\right)-2\pi}{3}\right) \\
\lambda_3 &= \tfrac{1}{3}K_1 + \frac{2K_1R_2}{3\sqrt{3-2R_2^2}}\cos\left(\frac{\arccos\left(R_3\right)+2\pi}{3}\right) \ .
\end{aligned} \tag{2.23}$$

CHAPTER 3

Tensor Shape Interpolation

3.1 Introduction and Related Work

Diffusion tensor shape and orientation properties are important components of computational models of cardiac mechanics and electrophysiology that require closely spaced nodes that do not necessarily lie at lattice points. DT-MRI data are, however, acquired at lattice points within a three-dimensional imaging volume, therefore tensor interpolation methods are needed.

The simplest tensor interpolation method is the Euclidean (EU) method, but it suffers from the swelling effects due to non-monotonic interpolation of tensor determinant (DET), and does not preserve the positive definiteness of diffusivity. The Riemannian approaches [Batchelor et al., 2005, Fletcher and Joshi, 2007, Lenglet et al., 2006, Pennec et al., 2006] overcome this problem, and more recently the log-Euclidean (LE) method [Arsigny et al., 2006] has been shown to be a computationally efficient approximation to the affine-invariant (AI) Riemannian approach [Pennec et al., 2006]. Kindlmann *et al.* [Kindlmann et al., 2007b] proposed a geodesic-loxodrome (GL) approach that guarantees monotonic interpolation of orthogonal tensor invariants, and demonstrated that the EU, AI and LE approaches fail to monotonically interpolate all the tensor invariants including tensor trace (TR), fractional anisotropy (FA) and tensor mode (MODE). The geodesic-loxodrome approach, however, is computationally expensive, and monotonic interpolation of the tensor invariants needs to be evaluated using experimen-

tally measured DT-MRI data. A Recent study has examined different methods to interpolate separately tensor shape and orientation. Yang *et al.* [Yang et al., 2012] proposed a method to resolve the sign ambiguity problem by finding the minimum rotation path between tensor orientations, but the minimum rotation path may not be the best way to resolve the sign ambiguity problem.

Firstly, we propose a new linear invariant (LI) tensor interpolation method, which linearly interpolates components of tensor shape (tensor invariants). We use the mathematics for converting the tensor invariants to eigenvalues to recapitulate the interpolated tensor from the linearly interpolated tensor invariants and the eigenvectors of a linearly interpolated tensor. The LI tensor interpolation method is simple to implement, fast, and perfectly commutative. Secondly, we determine which tensor interpolation scheme introduces the least microstructural bias to the shape and orientation of the interpolated tensors. To do so the LI tensor interpolation method is compared to the EU, AI, LE and GL methods of tensor interpolation using both a synthetic tensor field that reflects important myocardial tensor field attributes, and three experimentally measured DT-MRI datasets from rabbit, pig and human hearts.

3.2 Theory

A tensor invariant set composed of TR (K_1, magnitude-of-isotropy), FA (R_2, magnitude-of-anisotropy) and MODE (R_3, kind-of-anisotropy) fully decompose the shape of a tensor $\mathbf{D}$ defined in Eqs. 2.15 and 2.16.

Linear invariant (LI) interpolation of tensor $\mathbf{C}_{\mathrm{LI}}$ from tensors $\mathbf{A}$ and $\mathbf{B}$ with weighting coefficient $t \in [0, 1]$ starts by linearly interpolating the tensor invariants $J_j = \{K_1, R_2, R_3\}$:

$$J_j(\mathbf{C}_{\mathrm{LI}}) = (1 - t)J_j(\mathbf{A}) + tJ_j(\mathbf{B}) \ , \tag{3.1}$$

for $j = 1, 2, 3$. Then the mathematics for converting the tensor invariants into the

eigenvalues in Eq. 2.23 permits converting the tensor invariants $J_j(\mathbf{C}_{\mathrm{LI}})$ into the eigenvalues $\lambda_i(\mathbf{C}_{\mathrm{LI}})$.

To define the eigenvectors for $\mathbf{C}_{\mathrm{LI}}$, we use linear (EU) tensor interpolation:

$$\mathbf{C}_{\mathrm{EU}} = (1-t)\mathbf{A} + t\mathbf{B} \ , \tag{3.2}$$

then decompose $\mathbf{C}_{\mathrm{EU}}$ into the eigenvector and eigenvalue matrices $\mathbf{R}_{\mathrm{EU}}$ and Λ_{EU} where:

$$\mathbf{C}_{\mathrm{EU}} = \mathbf{R}_{\mathrm{EU}}\Lambda_{\mathrm{EU}}\mathbf{R}_{\mathrm{EU}}^{T} \ . \tag{3.3}$$

We can use AI, LE or GL tensor interpolation, but EU is the simplest and fastest, and introduces a similar bias in tensor orientation recovery, as will be shown later in Section 3.4.

Finally the interpolated tensor $\mathbf{C}_{\mathrm{LI}}$ is constructed using the eigenvalue matrix:

$$\Lambda_{\mathrm{LI}} = \mathrm{diag}\left(\lambda_i(\mathbf{C}_{\mathrm{LI}})\right) \tag{3.4}$$

from the linearly interpolated *tensor invariants*, and the eigenvector matrix $\mathbf{R}_{\mathrm{EU}}$ from the linearly interpolated *tensor*:

$$\mathbf{C}_{\mathrm{LI}} = \mathbf{R}_{\mathrm{EU}}\Lambda_{\mathrm{LI}}\mathbf{R}_{\mathrm{EU}}^{T} \ . \tag{3.5}$$

3.3 Methods

3.3.1 Synthetic Tensor Field

Using the EU, LE, GL and LI tensor interpolation methods, bilinear interpolation was performed between tensors that approximate the sheet shape of $(K_1, R_2, R_3) = (7, 0.6, 0.5)$ and fiber shape of $(6, 0.7, 1)$ observed in cardiac DT-MRI data, and range of tensor orientations.

3.3.2 Real Cardiac DT-MRI Acquisition

The rabbit heart DT-MRI data was acquired in a formalin fixed rabbit heart using a 7T Bruker Biospin scanner and a 3D fast spin echo sequence. Five non-diffusion weighted and twenty-five diffusion weighted (b-value $= 1000\,\mathrm{s/mm^2}$) imaging volumes were used to estimate the local $\mathbf{D}$ without zero padding and with linear regression. The imaging parameters were TE/TR $= 29.1/550\,\mathrm{ms}$, RARE factor two, FOV $= 35 \times 35 \times 35\,\mathrm{mm}$, and a $96 \times 96 \times 72$ encoding matrix – resulting in $365 \times 365 \times 528\,\mu\mathrm{m}$ spatial resolution. The porcine heart DT-MRI data was acquired using 2D multislice readout segmented EPI, similar encoding directions and reconstruction method with the following imaging parameters: TE/TR $= 80/6800\,\mathrm{ms}$, FOV $= 150 \times 150 \times 129\,\mathrm{mm}$, and an $150 \times 150 \times 43$ encoding matrix – resulting in $1 \times 1 \times 3\,\mathrm{mm}$ spatial resolution. The high-resolution human heart DT-MRI data was downloaded from Johns Hopkins University [Helm et al.]. The FOV was $110 \times 110 \times 110\,\mathrm{mm}$, the encoding matrix size was $256 \times 256 \times 134$, and the spatial resolution was $0.430 \times 0.430 \times 1.0\,\mathrm{mm}$.

3.3.3 Interpolation Evaluation

Each DT-MRI volume was segmented to identify the myocardium using thresholding and morphologic operations on the non-diffusion weighted image volume. To evaluate each interpolation method the measured ("truth") tensor volume was first downsampled in each direction by a factor of 2 for the rabbit and porcine heart data, and by a factor of 4 for the high-resolution human heart data. Subsequently tensors were trilinearly interpolated at the positions of the removed tensors using the remaining data. This permits a direct, paired comparison of the interpolated tensors to the "truth" tensors using data de-correlation and bootstrap statistics (see below). This comparison was made for six tensor scalar measures (TR, FA, MODE, DET, angle difference between primary eigenvectors, and log-Eugclidean

tensor distance [Arsigny et al., 2006]) computed at each location of the interpolated tensors using each of the tensor interpolation methods.

3.3.4 Tensor Statistics

The distributions of the six tensor scalar measures contain correlated data, are non-Gaussian, and have non-uniform variances. The use of ANOVA and t-test statistics, however, requires that the data in each population are not correlated, are Gaussian distributed (negligible skewness, kurtosis, etc.), and have similar variances; hence de-correlation and bootstrap methods are required.

3.3.5 De-correlation

The population of each tensor scalar measure was spatially decorrelated by computing the autocorrelation (AC) length for every dimension using the fully sampled data and the mask. For each of the $x-$, $y-$ and $z-$directions, all lines having at least four continuous myocardial points were found within the mask. For each line, the data values of the line were subtracted from their average, and then the AC sequence was computed. The AC length, which is the lag value at the first zero-crossing of the AC curve, was computed. The interpolated and original tensor data were conservatively decimated by the minimum integer value greater than or equal to all the median AC lengths for the tensor scalar measures in every dimension in order to spatially de-correlate the data.

3.3.6 Bootstrap Statistics

A paired comparison of each scalar tensor measure between the de-correlated interpolated tensors and the de-correlated original "truth" tensors was made using bootstrap methods. The population of paired differences between the scalar tensor measures (interpolated minus "truth" values) was computed, and 1000 ran-

domly resampled populations with replacement were constructed from the paired difference dataset. From each randomly resampled population the median was calculated. The 1000 median measures were sorted, and the asymmetric 95% confidence interval (CI) about the median was computed from the distribution for each tensor scalar measure. When this method is applied to paired angle differences between the primary eigenvectors or log-Euclidean tensor distances, only unsigned differences or distances can be computed. The median of the scalar tensor measure differences and the bootstrapped 95% CI of the median were compared to the zero-bias line (null hypothesis). If the paired differences are not significant, then the 95% Cl will overlap with the zero-bias line. When the paired difference CI does not overlap with the zero-bias line, then the respective tensor interpolation method introduces a significant bias to the tensor field.

3.4 Results

3.4.1 Synthetic Example

Figure 3.1 shows an example of bilinear interpolation between the four myocardial tensors at the vertices using the EU, LE, GL and LI methods. The tensors are visualized using superquadric glyphs [Ennis et al., 2005]. Each edge represents a microstructural transformation that can be observed both histologically and with DT-MRI. EU only monotonically interpolates TR. EU negatively biases FA and positively biases DET (i.e. the so-called tensor swelling effect [Arsigny et al., 2006]). LE negatively biases TR and FA, and only monotonically interpolates DET. Both EU and LE heterogeneously bias MODE. GL monotonically and LI linearly interpolate all the tensor invariants including DET. In order to establish that monotonic or linear interpolation of the tensor invariants is the best interpolation method, we evaluated each tensor interpolation method using the experimentally measured DT-MRI datasets as follows.

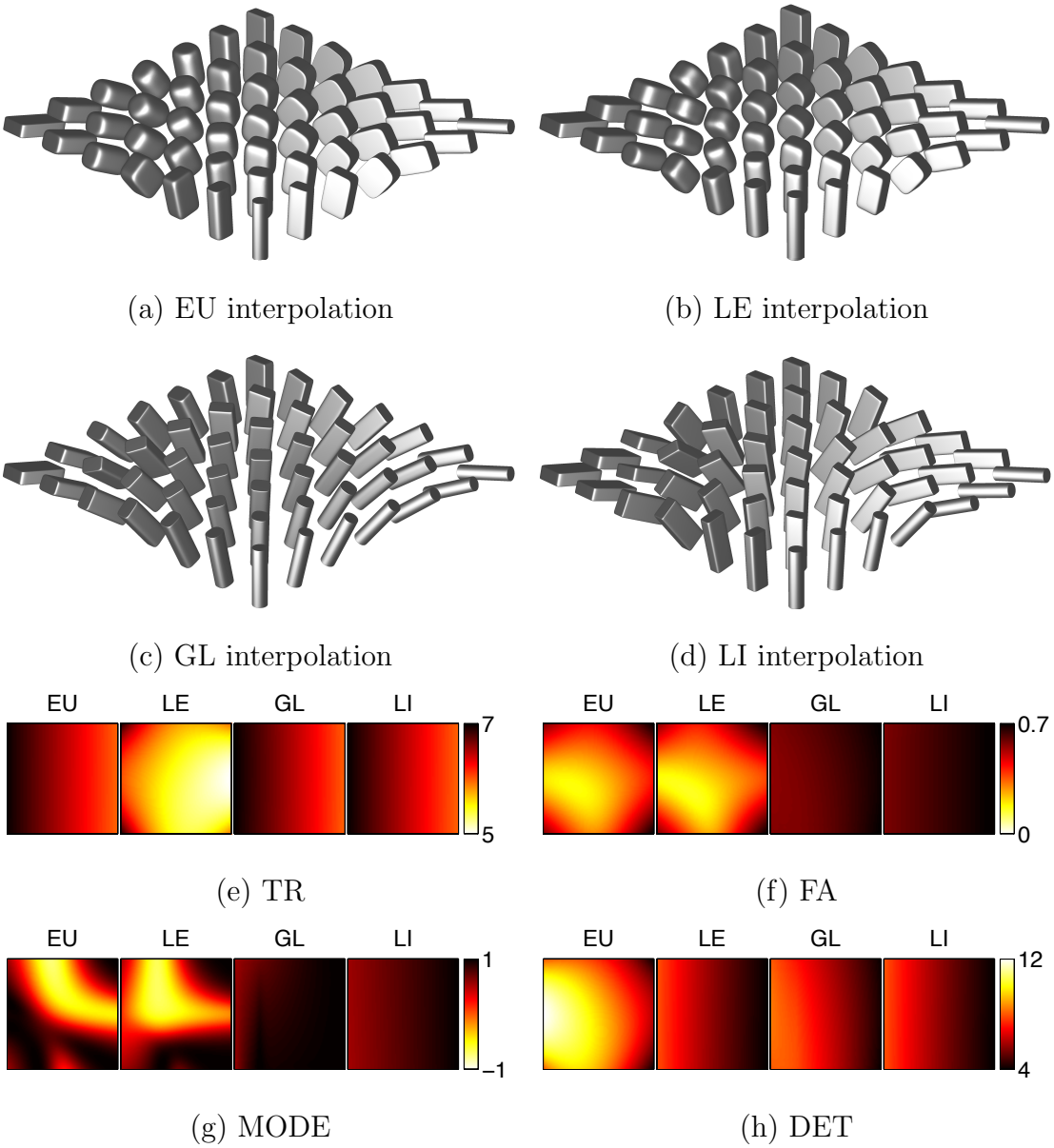

(a) EU interpolation

(b) LE interpolation

(c) GL interpolation

(d) LI interpolation

(e) TR

(f) FA

(g) MODE

(h) DET

Figure 3.1: Superquadric glyph rendering of the tensor field obtained from Euclidean (a), log-Euclidean (b), geodesic-loxodrome (c), and linear invariant (d) bilinear interpolation between the four myocardial tensors at the vertices. Maps of tensor trace (e), FA (f), tensor mode (g), and tensor determinant (h) from the resultant interpolated tensor fields are shown for each interpolation method. The front left edge in the tensor glyph images corresponds to the bottom of the tensor invariant images.

3.4.2 Autocorrelation

The AC procedure resulted in AC lengths of 3 in all the directions for the rabbit heart data; 4 in the $x-$ and $y-$directions, and 2 in the $z-$direction for the porcine heart data; and 8 in the $x-$ and $y-$directions, and 6 in the $z-$direction for the human heart data. To ensure that the data was de-correlated, the data was decimated by the AC length in each dimension.

3.4.3 Bootstrap Statistics

Figure 3.2 shows that EU does not introduce a significant bias to TR nor DET, but it does negatively bias FA and positively bias MODE. AI and LE are nearly identical and show a negative bias for TR, FA, and DET; and a positive bias for MODE. GL shows no significant bias for TR, FA, MODE, nor DET. LI does not introduce a significant bias for TR, FA, nor DET, but it does negatively bias MODE. All of the tensor interpolation methods produce an equivalent and positive bias for the primary eigenvector and the log-Euclidean tensor distance metric.

3.5 Discussion

The bootstrap comparison results demonstrate that GL and LI outperform EU, LE and AI in terms of tensor shape recovery. The bias introduced by AI and LE for recovery of TR and DET is a small ($\approx 2\%$) change relative to the absolute measures. Furthermore, current models do not make use of the TR information from the DT-MRI data because the conductivity tensor's eigenvalues have to be rescaled, hence this bias is not likely to be significant. The bias in FA introduced by EU, AI and LE is larger ($\approx 8\%$), and may significantly impact simulations when this data is incorporated into the computational model to rescale the conductivity

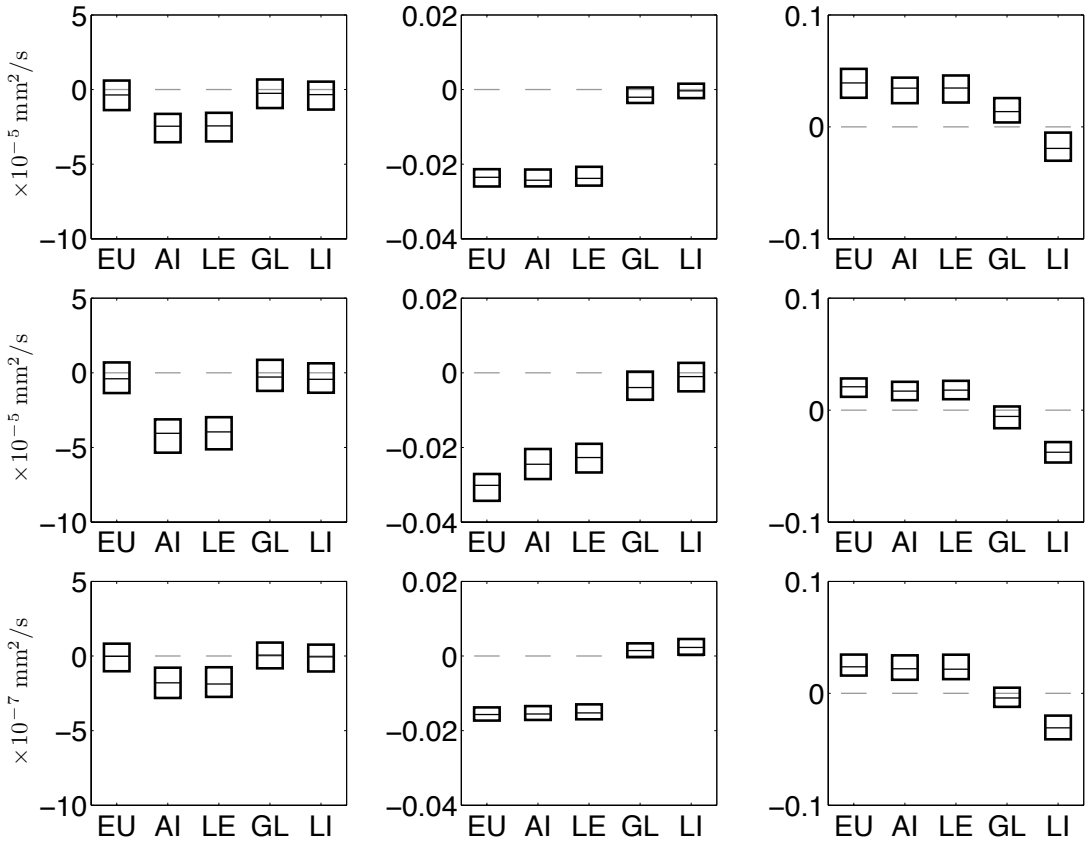

(a) Tensor trace (b) FA (c) Tensor mode

Figure 3.2: Continued on the next page.

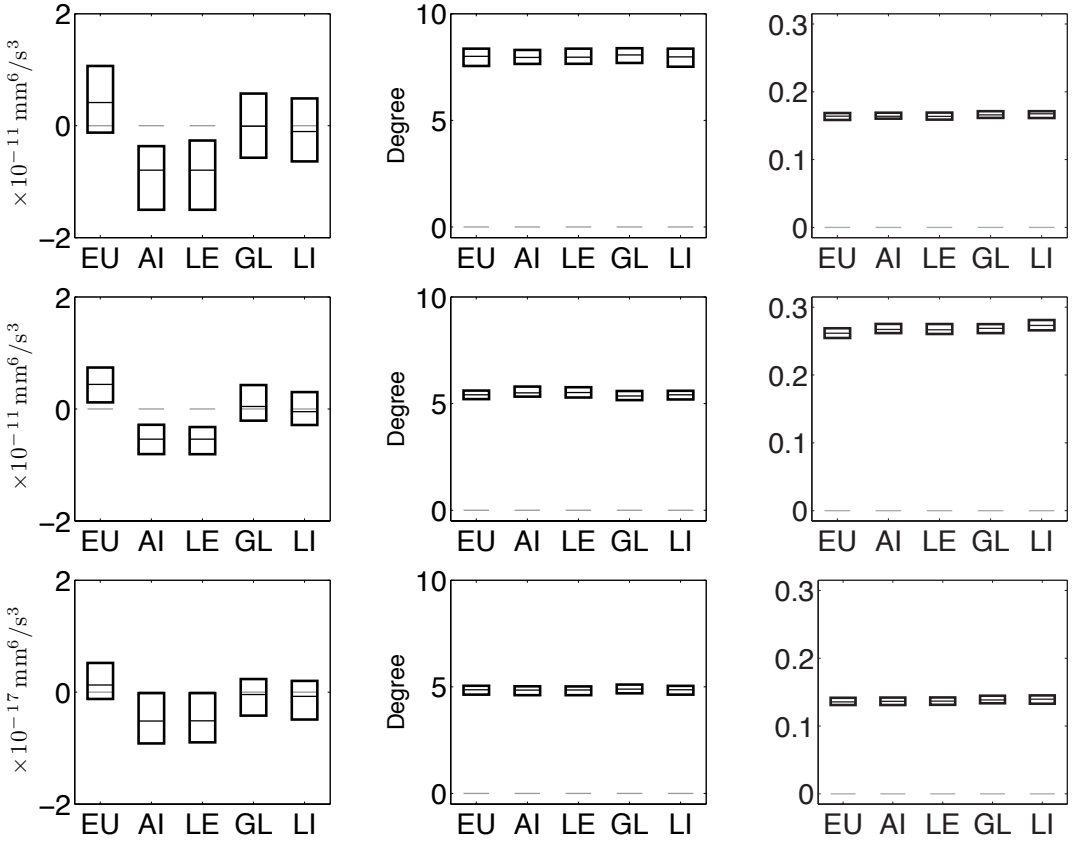

(d) Determinant (e) Primary eigenvector (f) LE distance

Figure 3.2: Bootstrap statistics for tensor measures. The upper row corresponds to the rabbit heart data, the middle row to the porcine heart data, and the lower row to the human heart data. Results of the paired comparison for tensor trace (a), FA (b), tensor mode (c), tensor determinant (d), angle difference between primary eigenvectors (e), and log-Euclidean tensor distance (f) are shown for each interpolation method. Each black horizontal line represents the median of each measure, and each box represents the bootstrapped 95% confidence interval of the median. The light gray horizontal lines at zero represent the zero bias.

tensor in regions of fibrosis and scar. Hence, accurate recovery of FA is important.

The magnitude of the bias in MODE by EU, AI, LE, and LI is similar ($\approx$ 4%). Only GL shows a distinct advantage as it interpolates MODE with no bias. Both electrophysiologic activation and mechanical tissue properties are known to be orthotropic, therefore accurate interpolation of MODE (lower bias) is likely beneficial.

For computational electrophysiology and mechanical modeling of the heart, orientation recovery is very important because the primary eigenvector (myofiber direction) strongly governs the direction of electrical activation and active contraction. All of the tested tensor interpolation methods introduce a $\approx 5^\circ - 8^\circ$ bias, which may introduce notable fiber "disarray" into computational models. A tensor interpolation method that better recovers tensor orientation is still needed.

The path interpolated by LI (respectively, GL) between two tensors lies in the 6-dimensional nonlinear manifold of tensors; this path has a projection onto the 3-manifold of tensor invariants (losing the directionality information). Here we interpolate on the 3-manifold, to linearly (respectively, monotonically) preserve the tensor shape attributes. The use of direct linear interpolation does not imply, nor is it motivated by, assumptions about global linearity, but naturally follows by considering the small neighborhood around a point to be homeomorphic to Euclidean space (valid for short distances), as given by the manifold structure. The paths are demonstrably close approximations of each other, and our fundamental ignorance of the true physical path on the tensor manifold makes it difficult to describe either LI or GL as "more meaningful." We therefore tested all the methods on real data.

In conclusion, if MODE recovery is important then GL should be used despite the computational cost. If MODE recovery is not critical then LI interpolation is an otherwise equivalent tensor interpolation method with reduced computational cost, which is important when interpolating tensors to the coordinates of 5 to 25

million computational nodes found in whole heart electrophysiology models. EU, AI, and LE tensor interpolation have no distinct advantage for the interpolation of tensor shape and orientation information based on the comparisons presented herein.

CHAPTER 4

Tensor Orientation Interpolation

4.1 Introduction

The second-order symmetric positive definite diffusion tensor ($\mathbf{D}$) can be decomposed into eigenvalues (λ_i, shape) and eigenvectors ($\mathbf{e}_i$, orientation). In cardiac applications, the three eigenvectors correspond to the myofiber long-axis ($\mathbf{e}_1$), the cross-fiber direction within the myolaminar sheet ($\mathbf{e}_2$) and the normal-sheet direction ($\mathbf{e}_3$) [Kung et al., 2011]. To build computational models of cardiac mechanics and electrophysiology (EP), both myofiber and myolaminae orientation information is required at millions of closely spaced nodes. DT-MRI measurements, however, are on a lattice and typically number $<$ 1e6 for *ex vivo* studies $<$ 1e4 for *in vivo* studies [Tseng et al., 1999], so interpolation of tensor orientation is needed.

The orientation (SO(3)) interpolation problem has been widely studied in the computer graphics literature. However the tensor orientation interpolation problem in DT-MRI is more challenging because eigenvectors have an arbitrary sign (physiologically and mathematically) so tensor orientation cannot be uniquely described.

Most of the conventional approaches have been tensor-based and amongst the simplest is the Euclidean (EU) method, but it suffers from the tensor shape swelling effect [Pennec et al., 2006, Arsigny et al., 2006]. The affine-invariant Riemannian (AI) and log-Euclidean (LE) tensor interpolation methods [Pennec

et al., 2006, Arsigny et al., 2006] were proposed to solve the tensor shape (tensor swelling) problem, but they underestimate other tensor invariants including tensor trace and FA [Gahm et al., 2012, Yang et al., 2012]. The geodesic-loxodrome (GL) method [Kindlmann et al., 2007b] guarantees monotonic interpolation of orthogonal tensor invariants [Ennis and Kindlmann, 2006], but is computationally expensive. The linear invariant (LI) method [Gahm et al., 2012] linearly interpolates tensor invariants (shape) at significantly reduced computational cost, but no new method for tensor orientation interpolation was presented. The tensor-based methods mostly focus on tensor shape interpolation, and no distinct advantage of the methods in tensor orientation has been reported [Gahm et al., 2012]. Recently a separate tensor interpolation method [Yang et al., 2012] was proposed that interpolates Euler angles or quaternions along the minimum rotation path between tensor orientations, but it was not quantitatively validated using cardiac DT-MRI data.

We propose a new dyadic-tensor based (DY) tensor orientation interpolation method that sidesteps the eigenvector sign ambiguity problem by interpolating between the dyadic tensors of eigenvectors with subsequent reduction to rank-1 dyadics and orthogonal matrices. We also revise and simplify the quaternion-based (QT) method [Yang et al., 2012], and evaluate it using cardiac DT-MRI data. The QT and DY tensor-based methods are compared to the tensor-based interpolation methods including EU, AI, LE and GL for accurate recovery of cardiac microstructural orientation using four experimentally measured DT-MRI datasets from rabbit and pig hearts.

4.2 Theory

4.2.1 Quaternion-based Interpolation

One approach to resolve the sign ambiguity problem of eigenvectors is to directly tackle it by choosing the minimum rotation path between tensor orientations. Tensor orientation is commonly represented by a rotation matrix $\mathbf{R}$ in Eq. 2.13, but can also be represented by a unit quaternion:

$$\mathbf{q} = a + bi + cj + dk = [a, b, c, d] \tag{4.1}$$

where

$$a^2 + b^2 + c^2 + d^2 = 1 \ . \tag{4.2}$$

Tensor orientation has four different descriptions intuitively represented by rotation matrices $\mathbf{R}_i$ defined in Eq. 2.17, which can be converted into unit quaternions $\mathbf{q}_i$:

$$\mathbf{q}_i = [a, b, c, d], [b, -a, d, -c], [c, -d, -a, b], [d, c, -b, -a] \ . \tag{4.3}$$

Then the minimum rotation path between two tensor orientations $\mathbf{R_A}$ and $\mathbf{R_B}$ can be determined by the maximum magnitude of inner products between fixed $\mathbf{q_A}$ and four different $\mathbf{q_B}$ (or between fixed $\mathbf{q_B}$ and four different $\mathbf{q_A}$). If the maximum value has a negative sign, the corresponding quaternion $\mathbf{q_B}$ (or $\mathbf{q_A}$) should be negated. Once the unit quaternions are uniquely determined, normalized linear interpolation (nlerp) is used:

$$\mathbf{q_C} = ((1-t)\mathbf{q_A} + t\mathbf{q_B}) \, / \|(1-t)\mathbf{q_A} + t\mathbf{q_B}\| \ , \tag{4.4}$$

which is computationally less expensive than spherical linear interpolation (slerp) [Blow, 2004]. The interpolated quaternion $\mathbf{q_C}$ is easily converted to a rotation matrix $\mathbf{R_C}$.

4.2.2 Dyadic Tensor-based Interpolation

Another approach is to sidestep the sign ambiguity problem by using dyadic tensors [Basser and Pajevic, 2000]. From Eq. 2.12, dyadic tensors of eigenvectors $\mathbf{e}_i$ are defined by:

$$\mathbf{E}_i = \mathbf{e}_i \otimes \mathbf{e}_i = \mathbf{e}_i \mathbf{e}_i^T \ . \tag{4.5}$$

Note:

$$\mathbf{e}_i \otimes \mathbf{e}_i = -\mathbf{e}_i \otimes -\mathbf{e}_i \ . \tag{4.6}$$

Dyadic tensors have rank 1, only one non-zero eigenvalue whose value is 1, and the corresponding eigenvector is exactly $\mathbf{e}_i$ or $-\mathbf{e}_i$. Interpolation between $\mathbf{R_A} = [\mathbf{e_{A}}_i]$ and $\mathbf{R_B} = [\mathbf{e_{B}}_i]$ starts with linear interpolation between their dyadic tensors:

$$\mathbf{F}_i = (1-t)\mathbf{E_{A}}_i + t\mathbf{E_{B}}_i \ . \tag{4.7}$$

Since $\mathbf{F}_i$ do not generally have rank 1, the nearest rank-1 dyadic tensor $(\mathbf{x} \otimes \mathbf{x})$ can be obtained by minimizing:

$$\begin{aligned} J(\mathbf{x}) &= \|\mathbf{F}_i - \mathbf{x} \otimes \mathbf{x}\|_F^2 \\ &= \mathrm{tr}\left\{(\mathbf{F}_i - \mathbf{x}\mathbf{x}^T)^T(\mathbf{F}_i - \mathbf{x}\mathbf{x}^T)\right\} \\ &= \mathrm{tr}\left\{\mathbf{F}_i^2 - 2\mathbf{F}_i\mathbf{x}\mathbf{x}^T + (\mathbf{x}\mathbf{x}^T)^2\right\} \\ &= \|\mathbf{F}_i\|_F^2 - 2\mathrm{tr}(\mathbf{x}^T\mathbf{F}_i\mathbf{x}) + \|\mathbf{x}\|^4 \ , \end{aligned} \tag{4.8}$$

where $\|\cdot\|_F$ denotes the Frobenius norm, and the derivative is:

$$J'(\mathbf{x}) = -4\mathbf{F}_i\mathbf{x} + 4\|\mathbf{x}\|^2\mathbf{x} \ . \tag{4.9}$$

By setting the derivative equal to zero, the eigenvalue equation:

$$\mathbf{F}_i\mathbf{x} = \|\mathbf{x}\|^2\mathbf{x} \tag{4.10}$$

is obtained, therefore the eigenvector $\mathbf{m}_i$ corresponding to the largest eigenvalue of $\mathbf{F}_i$ minimizes Eq. 4.8. Since the interpolation between dyadic tensors is separately

performed on each pair of eigenvectors, however, the matrix $\mathbf{M} = [\mathbf{m}_i]$ is not generally orthogonal. The orthogonal matrix closest to $\mathbf{M}$ can be obtained by minimizing:

$$w_1\|\mathbf{x}_1 - \mathbf{m}_1\|^2 + w_2\|\mathbf{x}_2 - \mathbf{m}_2\|^2 + w_3\|\mathbf{x}_3 - \mathbf{m}_3\|^2 \ , \tag{4.11}$$

where $[\mathbf{x}_i]$ is an orthogonal matrix, and w_i are the eigenvalues computed by the LI method described in Section 3.2, which assigns different weights to each eigenvector term according to the interpolated tensor shape. Equation 4.11 can be rewritten in a matrix form:

$$\begin{aligned}\|(\mathbf{M} - \mathbf{X})\mathbf{W}\|_F^2 &= \mathrm{tr}\left\{(\mathbf{MW} - \mathbf{XW})(\mathbf{MW} - \mathbf{XW})^T\right\} \\ &= \mathrm{tr}\left\{(\mathbf{MW})(\mathbf{MW})^T\right\} + \mathrm{tr}\left(\mathbf{XWW}^T\mathbf{X}^T\right) - 2\mathrm{tr}\left(\mathbf{MW}^2\mathbf{X}^T\right) \\ &= \|\mathbf{MW}\|_F^2 + \|\mathbf{W}\|_F^2 - 2\mathrm{tr}\left(\mathbf{MW}^2\mathbf{X}^T\right) \ ,\end{aligned} \tag{4.12}$$

where $\mathbf{X} \in \mathrm{O}(3)$ and $\mathbf{W}^2 = \mathrm{diag}(w_i)$. Minimizing Eq. 4.12 is achieved by maximizing:

$$\begin{aligned}\mathrm{tr}\left(\mathbf{MW}^2\mathbf{X}^T\right) &= \mathrm{tr}\left(\mathbf{U\Sigma V}^T\mathbf{X}^T\right) \\ &= \mathrm{tr}\left(\mathbf{V}^T\mathbf{X}^T\mathbf{U\Sigma}\right) \\ &\leq \mathrm{tr}\left(\mathbf{\Sigma}\right) \ ,\end{aligned} \tag{4.13}$$

where $\mathbf{U}$, $\mathbf{\Sigma}$ and $\mathbf{V}$ are obtained from the singular value decomposition (SVD) of:

$$\mathbf{MW}^2 = \mathbf{U\Sigma V}^T \ , \tag{4.14}$$

implying that Eq. 4.13 is maximized when:

$$\mathbf{V}^T\mathbf{X}^T\mathbf{U} = \mathbf{I} \ \Leftrightarrow \ \mathbf{X} = \mathbf{UV}^T \ . \tag{4.15}$$

Therefore the interpolated tensor orientation $\mathbf{R_C} = [\mathbf{e_{C}}_i]$ can be obtained by replacing the singular values with ones from the SVD of $\mathbf{MW}^2$. If the determinant of $\mathbf{R_C}$ is -1, $\mathbf{R_C}$ should be negated to be a right-handed rotation matrix.

4.3 Methods

4.3.1 Synthetic Tensors

Using the EU, LE, GL, quaternion-based (QT) and dyadic tensor-based (DY) methods, interpolation was performed between two tensors of the same shape ($\{K_1, R_2, R_3\} = \{1, 0.5, 0.8\}$), and different orientations whose angles between each pair of eigenvectors are 82°, 45° and 64°. LI described in Section 3.2 was used for tensor shape interpolation and combined with QT and DY for complete tensor interpolation.

4.3.2 Real DT-MRI Data

The rabbit heart DT-MRI data was acquired using a 7T Bruker Biospin scanner, and a 3D fast spin echo sequence with the following imaging parameters: TE/TR = 30/500 ms, b-value = 1000 s/mm^2, 24 diffusion gradient encoding directions, 6 nulls, and RARE factor two. The in-plane imaging resolution was 0.5×0.5×0.80 mm obtained by using a 96×96 encoding matrix, 72–96 slices and a 48×48×54–72 mm imaging volume. The pig heart DT-MRI data was acquired using a Siemens 1.5T Avanto and a 3T Trio scanner, and a 2D readout-segmented echo-planar pulse sequence with the following imaging parameters: TE/TR = 80/6800 ms, b-value = 1000 s/mm^2, 30 diffusion gradient encoding directions, one null, 15 readout segments, and 8-10 averages. The in-plane imaging resolution was 1×1×3 mm obtained by using an 150×150 encoding matrix, 43–44 slices and a 150×150×129–132 mm imaging volume. Diffusion tensors were estimated without zero padding and with linear regression.

4.3.3 Evaluation Procedure

The same tensor orientation evaluation procedure described in Section 3.3 was applied to the two rabbit and two pig heart DT-MRI datasets. The median autocorrelation (AC) length for every dimension was computed in each tensor invariant (J_i) map of the segmented myocardium. The myocardial tensor volume was downsampled in each dimension by a factor of the smallest integer not less than the median AC length for each tensor invariant map, and trilinear tensor orientation interpolation was performed with the EU, AI, LE, GL, QT and DY methods at the removed voxels using the remaining data. Then the interpolated tensor orientations by each method were compared to the originally measured data by computing the angle difference between each pair of eigenvectors. Subsequently the population of the angle difference data was spatially decorrelated by decimating the data in every dimension by the smallest integer not less than the AC lengths, and the decorrelated data was bootstrapped 1000 times by random sampling with replacement to compute the 95% confidence interval (CI) about the median.

4.4 Results

4.4.1 Synthetic Example

Figure 5.1 shows an example of interpolation between two synthetic tensors with the same shape and different orientations using the EU, LE, GL, LI+QT and LI+DY methods. Tensors are visualized as superquadric glyphs [Ennis et al., 2005], and plots of each eigenvector's angle relative to the leftmost tensor's orientation are shown along the interpolation paths. EU and LE fail to preserve the tensor shape during rotation, but GL, LI+QT and LI+DY maintain the tensor shape. With respect to tensor orientation, QT and DY monotonically interpolates

the angle of every eigenvector. The tensor-based methods (EU, LE and GL), however, fail to monotonically interpolate the angle of the secondary eigenvector.

DY's monotonic interpolation of each eigenvector needs to be more carefully investigated. Each method has a distinct interpolation path between tensor orientations, and QT's path is explicitly the minimum rotation path. Monotonic interpolation of eigenvectors and/or the minimum rotation path does not imply interpolation of tensor orientation with the least error. Therefore, we experimentally evaluated each method using real DT-MRI data.

4.4.2 Evaluation Statistics

The smallest integers not less than the median AC lengths were 2, 2 and 3 for the rabbit heart data and 3, 3 and 2 for the pig heart data in the x–, y– and z–directions, respectively. Figure 4.2 shows the bootstrap statistics of angle differences between each eigenvector pair of the original and interpolated tensor orientations. Each dot represents the median angle difference, and each error bar represents the bootstrapped 95% CI of the median. The (black, dark gray, and light gray) dashed lines represent the (lower, upper, and upper) limits of the CIs associated with the (primary, secondary, and tertiary) eigenvectors for the (QT, DY, and DY, respectively) methods, which help to determine whether or not the CIs of QT or DY overlap with others.

Comparison of the relative orientation errors between methods reveals that each method performs constsistently across the various data sets (e.g. errors decrease from GL to QT to DY). QT's tensor orientation median error, however, is significantly higher than all other methods (95% CI does not overlap) for the rabbit data, but not for the pig data. DY performs similarly to conventional tensor interpolation methods for recovering $\mathbf{e}_1$ in both rabbit and pig DT-MRI data.

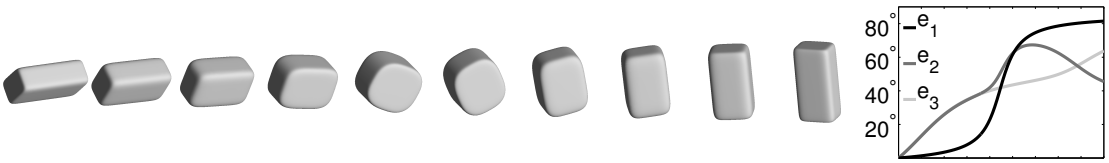

(a) Euclidean

(b) Log-Euclidean

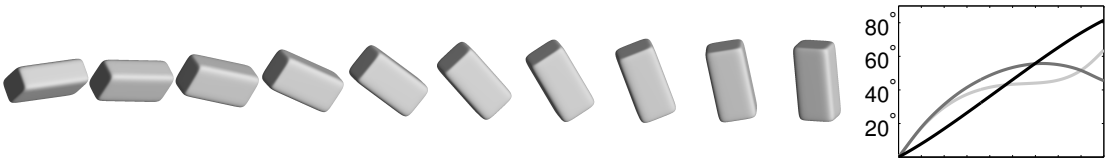

(c) Geodesic-loxodrome

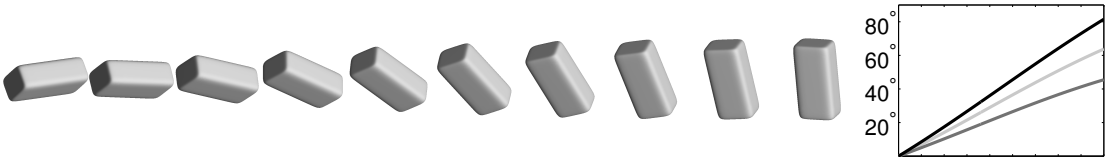

(d) Linear invariant + quaternion

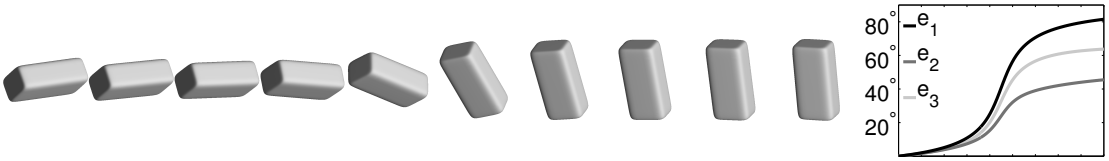

(e) Linear invariant + dyadic tensor

Figure 4.1: Interpolation between two synthetic tensors of equal shape and different orientation. The angle between every pair of the primary, secondary and tertiary eigenvectors is monotonically interpolated only in (d) and (e). All the tensor-based methods (a), (b) and (c) fail to monotonically interpolate the angle between the secondary eigenvectors.

DY has the lowest median error for recovery of both $\mathbf{e}_2$ and $\mathbf{e}_3$ compared to all other methods. Notably, DY has a significantly lower median recovery error for $\mathbf{e}_2$ and $\mathbf{e}_3$ compared either EU or GL for all four datasets.

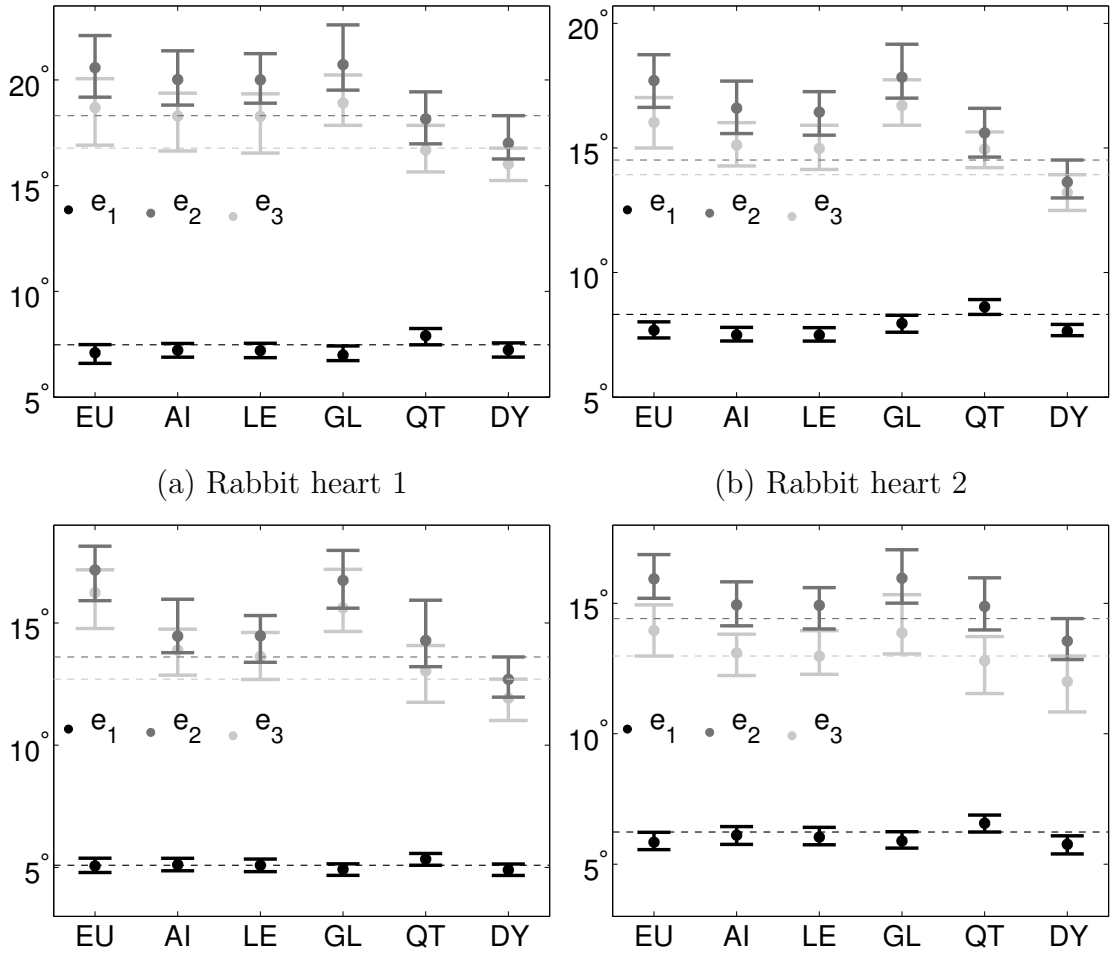

(a) Rabbit heart 1

(b) Rabbit heart 2

(c) Pig heart 1

(d) Pig heart 2

Figure 4.2: Bootstrap statistics for eigenvector orientation errors (angle differences) relative to real DT-MRI data. Each dot represents the median angle difference, and each error bar represents the bootstrapped 95% CI of the median. The (black, dark gray, and light gray) dashed lines represent the upper limits of DY's CIs associated with the (primary, secondary, and tertiary) eigenvectors, which define whether or not DY's CIs overlap with the others'. DY introduces the least error to the secondary and tertiary eigenvector orientations, and similar errors to the primary eigenvector orientation compared to the tensor-based methods (EU, AI, LE and GL).

4.5 Discussion

Accurate interpolation of myofiber and myolaminar sheet orientations is essential for computational modeling of cardiac mechanics and electrophysiology (EP). Cardiac mechanics and EP modeling requires accurate tensor orientation information at every computational node in order to assign correctly the axes of anisotropic electrical activation.

The comparison results show that DY performs significantly better than the tensor based methods, especially EU and GL, for recovery of each component of cardiac microstructural orientation. In particular, the improvement in recovery of the secondary and tertiary eigenvectors is important for recovery of myolaminar sheet orientation. Note that QT's minimum rotation path has significantly larger median errors for recovery of the primary eigenvector than DY's interpolation path.

LI+DY is a commutative, computationally efficient (compared to GL's numerical solution), and mathematically unambiguous tensor interpolation method that most accurately interpolates both cardiac microstructural shape [Gahm et al., 2012] and orientation. Further investigations using brain DT-MRI data and the same evaluation process may be needed to evaluate if the most accurate interpolation is dependent on the underlying tissue characteristics. Furthermore, the required tensor interpolation accuracy for cardiac mechanics and EP simulations remains incompletely understood.

CHAPTER 5

Weighted Component-based Tensor Distance

5.1 Introduction and Related Work

The examination of tissue microstructure using DT-MRI typically requires several post-processing tasks such as segmentation, registration, interpolation, analysis, and visualization that require appropriate tensor distance measurement [Wang and Vemuri, 2005, Pennec et al., 2006, Arsigny et al., 2006, Kindlmann et al., 2007b, Gahm et al., 2012]. The problem of tensor distance measurement was first approached using differences only in single scalar measures computed from diffusion tensors, ignoring differences in other tensor shape or orientation components. Amongst the simplest tensor distance metrics to measure both shape and orientation differences is the Euclidean metric, but it has been criticized for the swelling effect and lack of positive definiteness [Pennec et al., 2006, Arsigny et al., 2006]. To solve these problems, the Riemannian metrics [Pennec et al., 2006] were proposed based on sophisticated mathematics followed by the log-Euclidean metric [Arsigny et al., 2006], which is a computationally efficient approximation to the affine-invariant Riemannian metric. Another affine-invariant metric was proposed based on the J-divergence between two covariance matrices (tensors) [Wang and Vemuri, 2005].

These metrics only provide a single overall tensor distance with unknown, fixed contributions of shape and orientation distances between two tensors. Recently a new tensor interpolation path, termed geodesic-loxodrome, was proposed that

monotonically interpolates orthogonal tensor invariants, and separately measures distances in tensor shape and orientation [Kindlmann et al., 2007b]. The geodesic-loxodrome metric, however, is not practical when applied to large-scale processing jobs due to its expensive computational cost. More recently a computationally efficient approximate method described in Section 3.2 was proposed that linearly interpolates tensor invariants [Gahm et al., 2012]. The linearity of tensor invariants is not limited to tensor interpolation, and can be extended to tensor distance measurement.

We propose a new weighted component-based tensor distance that linearly combines tensor invariant (tensor trace, FA, and tensor mode) and orientation distances. This is accomplished, in part, by computing differences in each tensor invariant, and finding the minimum rotation between tensor orientations. Moreover the weighted component-based tensor distance allows users to adjust relative contributions of the invariant and orientation distance components toward an optimal single distance for a particular application. We apply the weighted component-based tensor distance to graph-based multi-label segmentation of DT-MRI of infarcted hearts with comparisons to the Euclidean, log-Euclidean [Arsigny et al., 2006], and J-divergence [Wang and Vemuri, 2005] metrics using a synthetic tensor field that reflects important myocardial tensor field attributes, and three experimentally measured DT-MRI datasets from post-infarct porcine hearts.

5.2 Theory

5.2.1 Tensor Invariant Distance

Tensor shape can be fully decomposed by a tensor invariant set $J_i = \{K_1, R_2, R_3\}$ composed of tensor trace (K_1), FA (R_2), and tensor mode (R_3) defined in Eqs. 2.15 and 2.16. Tensor invariant distances between two tensors $\mathbf{A}$ and $\mathbf{B}$ are achieved by simply computing the difference in each tensor invariant: $|J_i(\mathbf{A}) - J_i(\mathbf{B})|$ for

$i = 1, 2, 3$. Under the assumption of normal distribution with zero mean for each invariant distance (signed), the invariant distance is normalized by:

$$d_i(\mathbf{A}, \mathbf{B}) = |J_i(\mathbf{A}) - J_i(\mathbf{B})|/\sigma_i \ (i = 1, 2, 3) \ , \tag{5.1}$$

where σ_i is the standard deviation of the invariant distance population.

5.2.2 Tensor Orientation Distance

Tensor orientation $\mathbf{R}$ describes a rotation between the principal axes and a local coordinate system. Two arbitrary tensor orientations are also related by a rotation that can be used to define a distance between them. Since eigenvectors in DT-MRI may have an arbitrary sign, however, tensor orientation does not have a unique description; there may be four different rotations between the two orientations. Therefore, an orientation-specific tensor distance between $\mathbf{A}$ and $\mathbf{B}$ is achieved by finding the minimum rotation between their orientations $\mathbf{R_A}$ and $\mathbf{R_B}$, and normalizing it:

$$d_4(\mathbf{A}, \mathbf{B}) = \min_{\mathbf{P}} \arccos \left\{ \left(\mathrm{tr}(\mathbf{R_{AB}}) - 1 \right) /2 \right\} /\sigma_4 \ , \tag{5.2}$$

where

$$\mathbf{R_{AB}} = \mathbf{R_A P R_B}^T, \ \mathbf{P} = \mathrm{diag}([p_i]) \tag{5.3}$$

such that $p_i = \pm 1$ and $p_1 p_2 p_3 = 1$, and σ_4 is the standard deviation of the orientation distance population.

5.2.3 Graph-based Segmentation

The weighted component-based tensor distance is applied to graph-based multi-label segmentation of DT-MRI. Graph-based segmentation allows users to easily improve the segmentation results using their own expert knowledge without relying solely on the computational results. Given l user-defined seed voxels: l labeled $\{(\mathbf{x}_1, y_1), \cdots, (\mathbf{x}_l, y_l)\}$ and u unlabeled $\{\mathbf{x}_{l+1}, \cdots, \mathbf{x}_n\}$ voxels, where $\mathbf{x}$ represents

voxel's position vector and y is a label running from 1 to the number of classes (C), we construct an undirected weighted graph $G =< V, E, w >$ whose vertices $V = \{1, 2, \cdots, n\}$ correspond to all the voxels, and edges E represent similarities only between any pair of adjacent vertices p and q such that $\|\mathbf{x}_p - \mathbf{x}_q\| \leq \epsilon$ with edge weights $w_{p,q}$ defined by the Gaussian kernel with width σ:

$$w_{p,q} = \exp\left\{-d(\mathbf{D}_p, \mathbf{D}_q)^2/(2\sigma^2)\right\} \ , \tag{5.4}$$

where $d(\mathbf{D}_p, \mathbf{D}_q)$ is a distance based on any tensor distance metric between two tensors $\mathbf{D}_p$ and $\mathbf{D}_q$. Herein we define the weighted component-based tensor distance by a linear combination of the tensor invariant and orientation distances in Eqs. 5.1 and 5.2 with the weights α:

$$d(\mathbf{D}_p, \mathbf{D}_q) = \sum_{i=1}^{4} \alpha_i d_i(\mathbf{D}_p, \mathbf{D}_q) \ , \tag{5.5}$$

and the kernel width σ can be easily computed by:

$$\sigma^2 = \sum_{i=1}^{4} \alpha_i^2 \ . \tag{5.6}$$

Each σ_i in Eqs. 5.1 and 5.2 was adaptively set during the graph construction as:

$$\sigma_i^2 = \sum_{(p,q)\in\mathcal{N}} d_i(\mathbf{D}_p, \mathbf{D}_q)^2/|\mathcal{N}| \ , \tag{5.7}$$

where $\mathcal{N}$ represents the set of all the ϵ-neighborhoods.

Once the graph G has been built, the harmonic function, a popular graph-based multi-label segmentation algorithm, is used to estimate the undefined labels [Zhu et al., 2003]. Let $\mathbf{W}$ be the $n\times n$ graph weight matrix whose element is $w_{p,q}$, and $\mathbf{\Delta}$ be the $n\times n$ weighted degree matrix having only diagonal entries:

$$\mathbf{\Delta}_{p,p} = \sum_{q=1}^{n} w_{p,q} \ . \tag{5.8}$$

Then the Laplacian matrix $\mathbf{L}$ is defined as:

$$\mathbf{L} = \mathbf{\Delta} - \mathbf{W} \ , \tag{5.9}$$

and the $u \times C$ soft label matrix $\mathbf{f}_u$ for the unlabeled vertices is estimated by:

$$\mathbf{f}_u = -\mathbf{L}_{uu}^{-1}\mathbf{L}_{ul}\mathbf{Y}_l \ , \tag{5.10}$$

where $\mathbf{L}_{uu}$ and $\mathbf{L}_{ul}$ are the submatrices of $\mathbf{L}$ with the last u rows and columns and with the last u rows and first l columns, respectively, and $\mathbf{Y}_l$ is the $l \times C$ label indicator matrix whose ith row vector indicates the user-defined label y_i.

5.3 Methods

5.3.1 Synthetic Tensor Field

The weighted component-based tensor distance was evaluated over the Euclidean (Eucl), log-Euclidean (Log-Eucl), and J-divergence (J-div) distances on a four-label segmentation of a 90×90 synthetic tensor field that mimics a variety of diffusion tensors observed in cardiac DT-MRI data [Kindlmann et al., 2007a]. As observed from Fig. 5.1, the noise-free tensor field consists of four distinct materials: isotropic with low diffusivity (IsoLow, $J_i = \{0.4, 0, \text{n/a}\}$), isotropic with high diffusivity (IsoHigh, $J_i = \{1, 0, \text{n/a}\}$), linear anisotropic (Linear, $J_i = \{1, 0.7, 1\}$), and planar anisotropic (Planar, $J_i = \{1, 0.7, -1\}$) between which interfaces exist. Tensor orientation smoothly changes across the anisotropic regions, and does not change significantly around the boundaries. Therefore the ratio 2:1:1:0 was chosen as the weights α in Eq. 5.5. The parameter ϵ for the ϵ-neighborhood graph was set to 3 in all the experiments. Different levels of DT-MRI noise were simulated by corrupting the noise-free diffusion weighted images with Rician noise as described in Section 6.2.1 [Chang et al., 2007].

For the quantitative evaluation of the segmentation, the overall Dice coefficient (DC) was computed between two overlapping regions A and B as:

$$\text{DC}_{\text{overall}} = \frac{2\sum_i \beta_i |A_i \cap B_i|}{\sum_i \beta_i \left(|A_i| + |B_i|\right)} \tag{5.11}$$

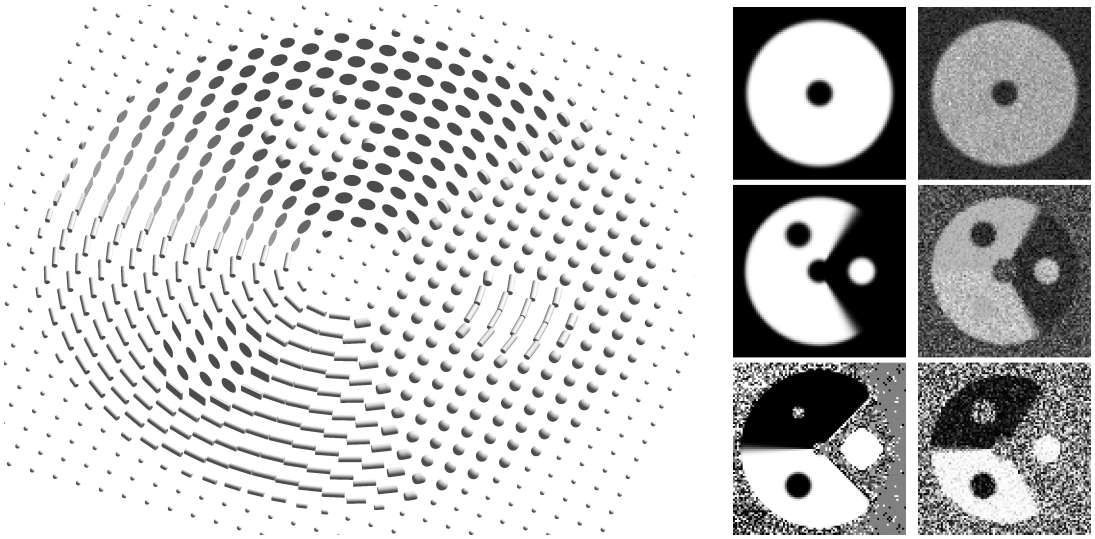

(a) Glyph rendering (b) Invariant maps

Figure 5.1: Synthetic tensor field. Superquadric glyph rendering (a) of the noise-free tensor field downsampled by a factor of 3 shows a range of tensor shape and orientation. Maps (b) of tensor trace (top), FA (middle), and tensor mode (bottom) for the noise-free (left) and noisy (SNR = 10, right) tensor fields show four distinct tensor shapes.

at each noise level with 512 independent instantiations of noise. β_i was chosen as the inverse of the average area of A_i and B_i so that all the labels equally contributed to the overall overlap.

5.3.2 Real Cardiac DT-MRI

DT-MRI data of the post-infarct porcine heart was acquired using a Siemens 1.5T Avanto or 3T Trio scanner, and a 2D readout-segmented echo-planar pulse sequence with the following imaging parameters: TE/TR = 80/6800 ms, b-value = 1000 s/mm^2, 30 diffusion gradient encoding directions, one null, 15 readout segments, BW = 439 Hz/pixel, and 8–10 averages. The in-plane imaging resolution was 1×1×3 mm obtained by using an 150×150 encoding matrix, 43–44 slices and

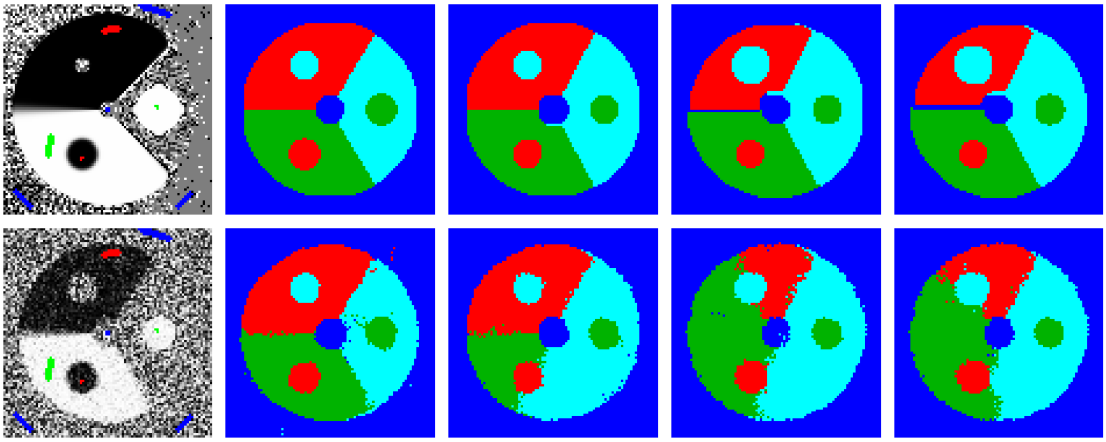

(a) Seed (b) Weighted (c) Eucl (d) Log-Eucl (e) J-div

Figure 5.2: Segmentation results for the noise-free (upper row) and noisy (SNR = 10, lower row) synthetic tensor fields. IsoLow (blue), IsoHigh (cyan), Linear (green), and Planar (red) regions were segmented using the seeds provided in the tensor mode images (a). Only the weighted component-based tensor distance (b) was successful for both the tensor fields.

an 150×150×129–132 mm imaging volume.

Segmentation of remote, border zone (BZ) and infarct regions in the pre-segmented myocardium was performed using the different tensor distance metrics. A recent study [Kung et al., 2012] showed that there was significant remodeling in BZ characterized by a large increase in tensor trace, an intermediate decrease in FA and a small decrease in tensor mode relative to normal and remote myocardium. The microstructural changes were largest in the infarct, which led us to choose the weights α = 8:4:1:1 in Eq. 5.5.

5.4 Results

Figure 5.2 shows the four-label segmentation results for the noise-free and noisy (SNR = 10) synthetic tensor fields. The weighted component-based tensor dis-

tance was successful even for the noisy tensor field, but the Euclidean, log-Euclidean and J-divergence distances all produced significant errors around boundaries between the three different parts within the high diffusivity regions of the noisy tensor field, and slight errors even for the noise-free tensor field.

Figure 5.3 shows statistics of the segmentation results using the same seeds over a different level of noise for the synthetic tensor field. The weighted component-based tensor distance produced the best accuracy with small variations for SNR ≥ 5, and the Euclidean distance also showed good accuracy for intermediate to high SNR. However, the log-Euclidean and J-divergence distances produced poor accuracy with highly significant variations in the high diffusivity regions even for high SNR, and accuracy and robustness were even worse for the planar anisotropic part within the high diffusivity regions.

Figure 5.4 shows segmentation of remote, BZ and infarct regions in the pre-segmented myocardium on a slice from each of the three different DT-MRI datasets of post-infarct porcine hearts. Tensor trace images are shown for reference and highlight the scar. BZ regions wherein viable myocardium and fibrotic scar are mixed are expected as a thin layer between remote and infarct regions. The weighted component-based tensor distance yielded the best segmentation results corresponding to our expectation for all the experiments, and the Euclidean metric produced good accuracy only for infarct regions. However, the log-Euclidean and J-divergence metrics significantly overestimated BZ and infarct regions, and would require much more time and effort in seed selection to obtain a similar result.

5.5 Discussion

The log-Euclidean and J-divergence metrics are based on solid mathematics, but have no distinct advantage for tensor-based segmentation based on the results presented herein. The weighted component-based tensor distance is simple, but

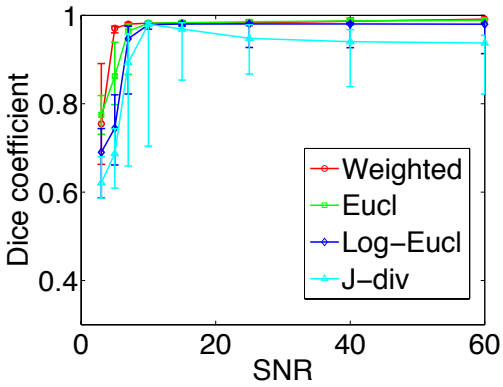

(a) IsoLow

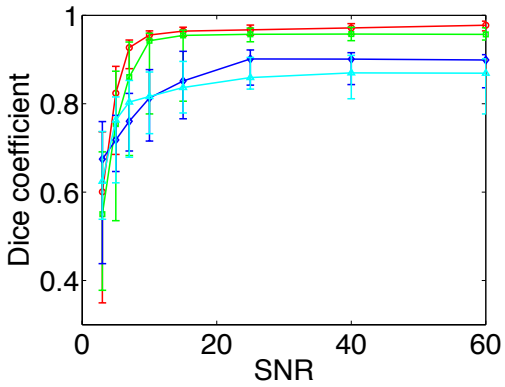

(b) IsoHigh

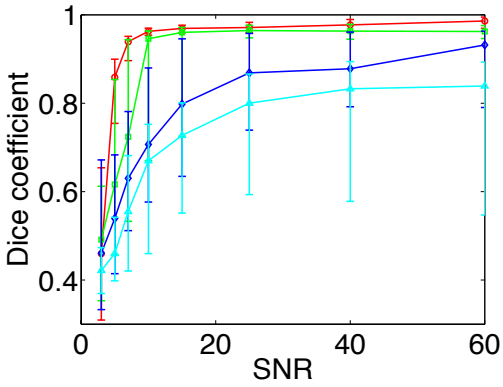

(c) Linear

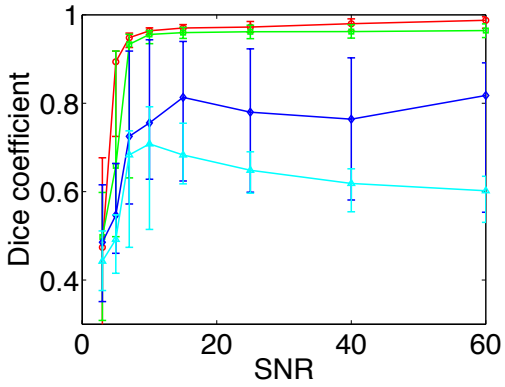

(d) Planar

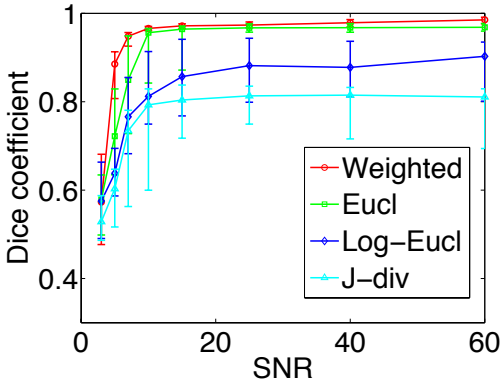

(e) Overall

Figure 5.3: Statistics of segmentation results over different levels of noise for the synthetic tensor field. Each central mark and error bar indicates the median and the 2.5 and 97.5 percentiles of the Dice coefficient population for 512 independent noisy experiments. The weighted component-based distance produced the highest accuracy with small variations for all the labels.

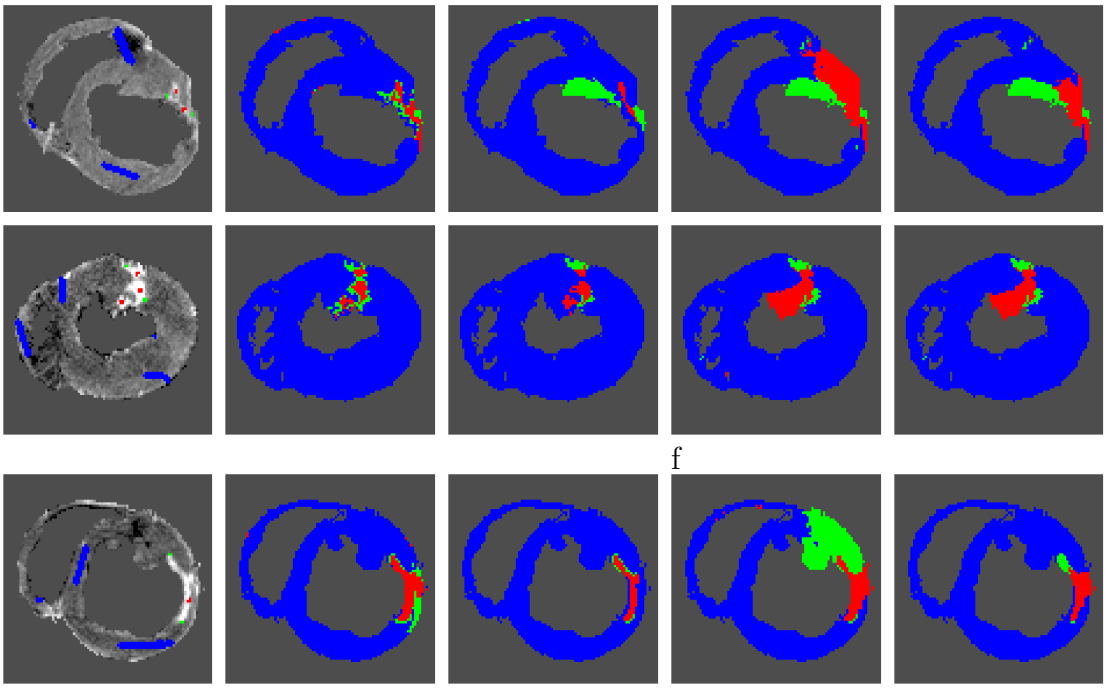

(a) Seed (b) Weighted (c) Eucl (d) Log-Eucl (e) J-div

Figure 5.4: Segmentation results for the three real DT-MRI datasets different in row. Remote (blue), BZ (green), and infarct (red) regions were segmented from the pre-identified myocardium using the seeds provided in tensor trace images (a). The weighted component-based distance (b) identified BZ and infarct regions closest to the expected size and shape.

more powerful because contributions from tensor invariant and orientation distance components can be adjusted according to a particular application.

The weights used to determine the relative impacts on the overall distance can be chosen by investigating the contrast in each tensor invariant and orientation map, and empirically adapted to the optimal values. Once the optimal weights are found for one dataset in a particular study, we expect that the same weights will also work for different datasets from within the same study as shown in our experiments with the different DT-MRI datasets of post-infarct porcine hearts. Future work includes providing the weights for other applications based on statis-

tical grounds to avoid the process of manual selection of the parameters that may bias further statistical studies.

Lack of data and the difficulty of finding the ground truth segmentation do not allow statistical evaluation of the weighted component-based tensor distance on segmentation of BZ and infarct regions. Microstructural remodeling in BZ and infarct regions has been of great interest as it may clarify microstructural requirements that lead to ventricular arrhythmogenesis. Importantly, to build computational models of electrophysiology a microstructural based segmentation is required. The weighted component-based tensor distance is not limited to this graph-based segmentation of infarct myocardium, and can be applied to other DT-MRI applications or segmentation techniques.

CHAPTER 6

The Effects of Noise Over the Complete Space of Diffusion Tensor Shape

6.1 Introduction and Related Work

In the field of DT-MRI tensor invariants are the preferred means for characterizing tensor shape and are considered to report salient, if not intuitive, properties of the underlying diffusive process (magnitude of isotropy, magnitude of anisotropy, kind of anisotropy)[Basser et al., 1994b, Ennis and Kindlmann, 2006]. In fact, our understanding of, for example, FA has become so essential to the interpretation of DT-MRI data that the field must examine how the imaging protocol (b-value, number of gradient directions, k-space encoding scheme etc.) and the image signal-to-noise ratio (SNR) impact measures of FA. This has, of course, been performed but under a relatively narrow and constrained range of tensor shape, wherein an assumption of cylindrically symmetric anisotropy was used [Pierpaoli and Basser, 1996, Jones, 2004]. This assumption, though convenient, is not necessary and limits the range of tensor shape that has been investigated. Previous studies have evaluated the impact of noise on specific asymmetric tensors [Basser and Pajevic, 2000] and specific diffusion tensors representative of the brain [Chang et al., 2007], but the effects of noise over a wide range of tensor shapes has not previously been considered.

Furthermore, previous analyses of the impact of noise on diffusion tensor invariants have only considered how the invariants become statistically distributed

in the presence of complex noise added to the image domain - a framework that we term the "Forward Problem." This stands in distinction to the situation we encounter experimentally wherein we are presented with a measured tensor invariant and we are concerned with the true value of the tensor invariant given that we know it is corrupted by a level of noise that is measurable in the non-diffusion weighted image(s). We term this framework the "Inverse Problem."

We evaluate by simulation the effects of noise on characterizing tensor shape over the complete space of tensor shape for three encoding schemes with different SNR and gradient directions. We also define the new framework "Inverse Problem" for determining the distribution of the true values of tensor invariants given their measures, which provides guidance about the confidence the observer should have in the measures. Finally, we present the statistics of tensor invariant estimates over the complete space of tensor shape to demonstrate how the noise sensitivity of tensor invariants varies across the space of tensor shape as well as how the imaging protocol impacts measures of tensor invariants.

6.2 Methods

6.2.1 DT-MRI Noise Simulations

DT-MRI noise simulations similar to those described in [Pierpaoli and Basser, 1996, Jones, 2004, Chang et al., 2007] were performed to evaluate the effects of noise on tensor shape over the complete space of diffusion tensor shape. Because of the prevalence in the literature that reports tensor trace and FA, we first constructed a single diffusion tensor $\mathbf{D}$ from a tensor invariant set $\{K_1, R_2, R_3\}$ using Eq. 2.23 over the complete range of tensor trace (K_1), FA (R_2), and tensor mode (R_3) (see Sections 6.2.3 and 6.2.4). The laboratory frame in which the diffusion tensor is represented was assumed to coincide with the principal frame for simplicity ($\mathbf{R} = \mathbf{I}$ in Eq. 2.13). This initial, noise-free tensor is termed the "truth"

tensor ($\mathbf{D}_\mathrm{T}$) because it serves as ground truth for quantifying variability subject to the addition of noise.

Next we generated the noise-free diffusion weighted (DW) signal intensities (S_j) through the Stejskal-Tanner equation [Stejskal and Tanner, 1965]:

$$S_j = S_0 e^{-b_j \mathbf{g}_j \cdot \mathbf{D} \mathbf{g}_j} \ , \tag{6.1}$$

where S_j is the jth measured real-valued signal with diffusion weighting, S_0 is the non-diffusion weighted real-valued signal (chosen as a constant for all simulations), b_j is the b-value, and $\mathbf{g}_j$ is the gradient sampling direction unit vector. We used the Jones 6-direction ($\mathrm{N_{Dir}}$=6) scheme plus one null ($\mathrm{N_{Null}}$=1), and the Jones 30-direction ($\mathrm{N_{Dir}}$=30) scheme plus five nulls ($\mathrm{N_{Null}}$=5) with b-value=[0,1000] s/mm^2[Jones et al., 1999, Skare et al., 2000]. The diffusion encoding gradient directions were not repeated.

To simulate noisy S_j we added a complex random number whose real and imaginary parts were independent and Gaussian distributed with mean zero and standard deviation σ [Henkelman, 1985]:

$$\sigma = \frac{S_0}{\sqrt{\mathrm{SNR}^2 - 1}} \ . \tag{6.2}$$

The magnitude of the noisy signals was then used to reconstruct noisy diffusion tensor estimates $\mathbf{D}_\mathrm{N}$ using linear least squares regression from Eq. 6.1.

Simulations were performed with SNR=10 and SNR=25. We refer to each experimental combination as an SNR–$\mathrm{N_{Dir}}$+$\mathrm{N_{Null}}$ encoding scheme (e.g. 10–30+5 for SNR=10, $\mathrm{N_{Dir}}$=30, and $\mathrm{N_{Null}}$=5). Simulations were performed for three encoding schemes: 10–30+5, 25–30+5, and 25–6+1.

6.2.2 Data Representation

The multivariate nature of the simulation (SNR, encoding schemes, and invariant ranges) necessitates a careful reduction of this space to salient representations.

Note that the three-dimensional space of symmetric positive definite tensors in the principal coordinate frame span a planar isosurface when tr$\mathbf{D}$ is constant (Fig. 6.1A). Furthermore, the sorted eigenvalues ($\lambda_1 \geq \lambda_2 \geq \lambda_3$) form a barycentric space that occupies $1/6^{th}$ of this space. We use this eigenvalue subspace to depict the results of the noise perturbation simulations at intersections of the iso-R_2 arcs and iso-R_3 rays (Figs. 6.1B and 6.1C). These values were chosen because they represent uniform steps in the eigenvalue coordinates, but note that the R_2 and R_3 steps are non-uniform.

6.2.3 Forward Problem

The Forward Problem defines the statistical distribution of the noisy tensor invariants for a "truth" tensor ($\mathbf{D}_\mathrm{T}$) when complex Gaussian noise is added to S_j and S_0 using the procedure in Section 6.2.1. This results in the forward propagation of noise $\mathbf{N}_i$ producing the noise-corrupted tensor $\mathbf{D}_{\mathrm{N},i}$:

$$\mathbf{D}_{\mathrm{N},i} = \mathbf{D}_\mathrm{T} + \mathbf{N}_i \ . \tag{6.3}$$

128^2 noisy tensors were generated for each $\mathbf{D}_\mathrm{T}$ and used to define a distribution of noisy R_2 and R_3 invariants using Eq. 2.16 for one SNR–$\mathrm{N_{Dir}}$+$\mathrm{N_{Null}}$ encoding scheme. Figure 6.1B demonstrates this process for $\mathbf{D}_\mathrm{T}$ with $\{K_1, R_2, R_3\} = \{2.1$ $\mu\mathrm{m}^2/\mathrm{ms}$, 0.47, 0$\}$ and the 10–30+5 encoding scheme, where each instance of the noisy invariants is represented as a dark gray dot. Three examples of the noisy invariants that generate $\mathbf{D}_{\mathrm{N},i}$, $\mathbf{D}_{\mathrm{N},i+1}$ and $\mathbf{D}_{\mathrm{N},i+2}$ demonstrate the possible effects of the forward propagation of noise on an individual tensor as in Eq. 6.3. The curved arrows represent the noise propagation. The bias of the noisy invariant distribution is represented as a straight arrow pointing from the invariant coordinates used to generate $\mathbf{D}_\mathrm{T}$ to the median of the noisy invariant distribution that generates $\bar{\mathbf{D}}_\mathrm{N}$. Noisy tensors with negative eigenvalues, which can arise, for example, when noise levels are high relative to the smallest eigenvalue were included

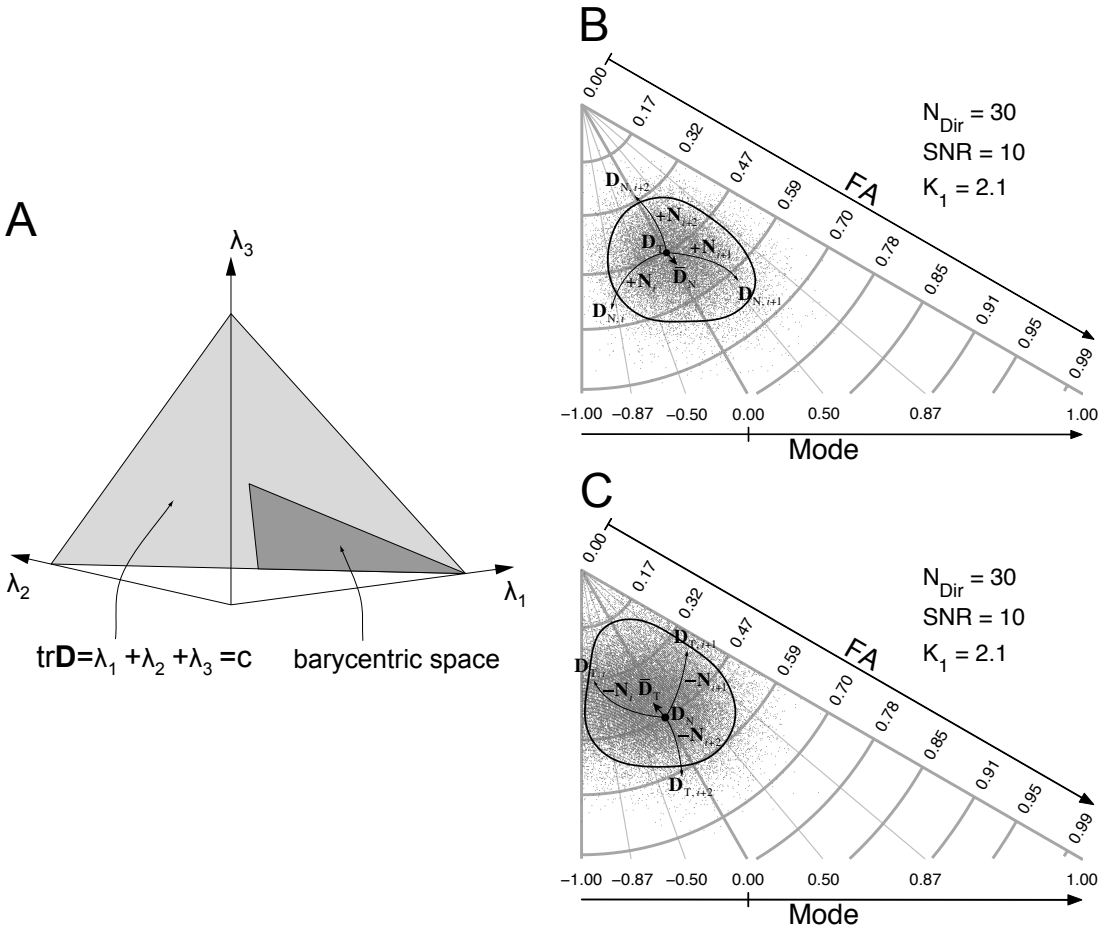

Figure 6.1: (A) Triangular isosurface (light gray) of constant (c) tensor trace over the three-dimensional space of symmetric positive definite tensors in the principal coordinate frame. The eigenvalues form a barycentric space (dark triangle). (B, C) Barycentric space highlighted with iso-FA arcs and iso-mode rays. (B) depicts the forward propagation of noise $\mathbf{N}_i$ from a truth tensor $\mathbf{D}_\mathrm{T}$ producing the noise-corrupted tensor $\mathbf{D}_{\mathrm{N},i}$. (C) depicts the inverse propagation of noise $\mathbf{N}_i$ from a noisy tensor $\mathbf{D}_\mathrm{N}$ producing the noise-free tensor $\mathbf{D}_{\mathrm{T},i}$.

to define completely the statistical distributions of invariants.

This process was repeated to discretely span the complete space of R_2 and R_3 by calculating $\mathbf{D}_\mathrm{T}$ from Eq. 2.23 such that K_1 was fixed at one value in

$[0.6, 2.1, 7.2]$ μm^2/ms, which represents the low trace of lymphoma [Barajas et al., 2010], nominal trace in the brain parenchyma [Maier et al., 1998], and the high trace of free water, respectively. R_2 and R_3 were chosen to fall at the intersection of the iso-R_2 arcs and iso-R_3 rays in Fig. 6.1B.

Spanning the complete space of tensor shape was sufficiently achieved by discretely varying K_1 between very low, nominal and very high values. The effects of noise on K_1 were less complex and relatively independent of R_2 and R_3 (see Sections 6.3.1 and 6.3.2). It is inherently difficult to produce figures that display information over more than two degrees-of-freedom. Therefore we projected them onto a 2D space of constant K_1 to elucidate the more complex effects of noise on R_2 and R_3 (Fig. 6.1).

6.2.4 Inverse Problem

Experimentally we always measure noisy data. Therefore, it is useful to define the statistical distribution of *possible* $\mathbf{D}_\mathrm{T}$ that could have given rise to the measured (i.e. observed) invariants for a particular and known encoding scheme (SNR–$\mathrm{N_{Dir}}$+$\mathrm{N_{Null}}$). We use the term "Inverse Problem" to describe this scenario. Stated another way, when observing a particular tensor invariant value in our measured data the statistical results of the Inverse Problem provide guidance about the confidence the observer should have in the data, provided that the SNR–$\mathrm{N_{Dir}}$+$\mathrm{N_{Null}}$ is known.

The Inverse Problem was formulated by generating $\mathbf{D}_\mathrm{T}$ from Eq. 2.23 for all combination of densely sampled K_1, R_2 and R_3 values. K_1 was densely sampled around each value in $[0.6, 2.1, 7.2]$ μm^2/ms with the interval of $1/100$ μm^2/ms, that is, $K_1 = [0.1, 0.11, \ldots, 1.1] \cup [1.6, 1.61, \ldots, 2.6] \cup [6.7, 6.71, \ldots, 9.3]$ μm^2/ms, and the individual complete ranges of R_2 and R_3 were then divided into 400 intervals equally spaced in the eigenvalue coordinates, resulting in $7.45e7$ different $\mathbf{D}_\mathrm{T}$.

Then, 1,024 noisy tensors were generated at each of the 7.45e7 $\{K_1,R_2,R_3\}$ coordinates using the procedure in Section 6.2.1. This resulted in the generation of 7.62e10 noisy tensors that densely span the complete space of K_1, R_2 and R_3 with uniform steps of each invariant in the eigenvalue coordinates. This procedure avoids skewing the distribution as may occur with undersampling or non-uniform sampling. The K_1, R_2 and R_3 invariants were then computed for the noisy tensors.

Next, we found noisy tensors with K_1, R_2 and R_3 values within a small rectangular box with dimensions equals to two times the sampling intervals centered at the intersection of the iso-R_2 arcs and iso-R_3 rays and with K_1 fixed at one value in $[0.6, 2.1, 7.2]$ μm^2/ms. This population of the noisy tensors were grouped to form $\mathbf{D}_\mathrm{N}$, and inversely mapped to the original "truth" tensors $\mathbf{D}_\mathrm{T}$. Stated another way, each $\mathbf{D}_\mathrm{N}$ maps to an underlying tensor $\mathbf{D}_{\mathrm{T},i}$ by eliminating the noise $\mathbf{N}_i$:

$$\mathbf{D}_{\mathrm{T},i} = \mathbf{D}_\mathrm{N} - \mathbf{N}_i \ , \tag{6.4}$$

which can be done with a look-up table. Figure 6.1C demonstrates this process for $\mathbf{D}_\mathrm{N}$ with $\{K_1, R_2, R_3\} = \{2.1\ \mu\mathrm{m}^2/\mathrm{ms},\ 0.47,\ 0\}$ and the 10–30+5 encoding scheme, where each instance of the truth invariants is represented as a dark gray dot. Three examples of the truth invariants that generate $\mathbf{D}_{\mathrm{T},i}$, $\mathbf{D}_{\mathrm{T},i+1}$ and $\mathbf{D}_{\mathrm{T},i+2}$ demonstrate the possible effects of the inverse propagation of noise on an individual tensor as in Eq. 6.4.

The bias of the truth invariant distribution is represented as a straight arrow pointing from the invariant coordinates used to generate $\mathbf{D}_\mathrm{N}$ to the median of the truth invariant distribution that generates $\bar{\mathbf{D}}_\mathrm{T}$.

6.2.5 Confidence Interval

In order to evaluate the effects of the forward and inverse propagation of noise on characterizing tensor shape, we statistically compared: 1) the population of

noisy tensor invariants obtained from $\mathbf{D}_\mathrm{N}$ to the known tensor invariant of the respective $\mathbf{D}_\mathrm{T}$ tensor; and 2) the population of tensor invariants obtained from $\mathbf{D}_\mathrm{T}$ that gave rise to the noisy $\mathbf{D}_\mathrm{N}$ tensor. This was done for each of the three encoding schemes over the complete space of tensor shape. The statistical analysis compares the bias and 95% confidence interval (95%-CI) of the population to $\mathbf{D}_\mathrm{T}$ (Forward Problem) or $\mathbf{D}_\mathrm{N}$ (Inverse Problem).

The resultant distribution of invariants is represented as a bias and a surrounding 95%-CI contour projected onto an iso-K_1 plane. The bias represents the median offset of the distribution and the 95%-CI represents the band of confidence in the estimate of the bias. When two 95%-CI contours overlap there is a significant likelihood that the two $\mathbf{D}_\mathrm{T}$ (Forward Problem) or $\mathbf{D}_\mathrm{N}$ (Inverse Problem) tensors can not be distinguished. The median of the invariant distribution was achieved by computing the median value of each invariant, converting the median invariants to eigenvalues using Eq. 2.23, and projecting them onto a plane of constant K_1 equivalent to the barycentric space in Fig. 6.1.

The noisy R_2 and R_3 distribution generated in Section 6.2.3 and the truth R_2 and R_3 distribution generated in Section 6.2.4 are not bivariate Gaussian, therefore we cannot compute 95%-CI contours as simple ellipses. Consequently, the R_2 and R_3 samples were converted to samples of eigenvalues using Eq. 2.23. These eigenvalues were projected onto a plane of constant K_1 equivalent to the barycentric space in Fig. 6.1. Then, for each of 100 rays in the barycentric space at uniform angular intervals passing through the median of the samples, we found all of the samples falling within a narrow band ($\pm 1\%$ of the K_1 used for the respective simulation) around the ray. These values were projected onto the ray and used to calculate the 95%-CI by sorting these 1-D values and truncating the lowest and highest 2.5^{th}, thereby retaining 95% of the estimates.

We finally approximated the 95%-CI contour by fitting a periodic b-spline to the 200 (2 points for 100 rays) 95%-CI points with 10 control points. These

splines permit smooth approximation of the 95%-CI contours, and are shown as black closed splines in Figs. 6.1B (Forward Problem) and 6.1C (Inverse Problem).

6.3 Results

Two important theoretical results arise in this work. First, Eq. 2.23 provides a principled and analytic method to establish tensor shape attributes by using the tensor invariants to define the tensor's eigenvalues. This development precludes the need to assume cylindrically symmetric anisotropy as has been done previously [Pierpaoli and Basser, 1996, Jones, 2004, Chang et al., 2007], or the use of *ad hoc* methods to define eigenvalues that happen to have the desired tensor invariants. Secondly, the defining of the Inverse Problem and the subsequent result provides a new perspective on interpreting measured diffusion tensor invariant data. The application of these theoretical developments permits a description of the bias and 95%-CI that noise introduces in both the Forward and Inverse Problems over the complete space of tensor shape.

6.3.1 Effect of Noise in the Forward Problem

Effect of SNR. The effect of noise alone in the Forward Problem is demonstrated in Figs. 6.2A and 6.2B. For SNR=10 (10–30+5) the magnitude of the bias is increased and the 95%-CIs are substantially larger when compared to SNR=25 (25–30+5). In particular, note that the bias for SNR=10 (10–30+5) points toward increased FA and less extreme tensor mode. The bias toward higher FA is highest for $\mathbf{D}_{\mathrm{T}}$ with low FA and diminishes in magnitude almost entirely as the FA of $\mathbf{D}_{\mathrm{T}}$ increases. Note that the step-size of FA along the FA-axis decreases in the eigenvalue space, therefore moderate changes in eigenvalues result in very small increases in FA as FA $\rightarrow 1$. The bias in FA is relatively uniform across the complete range of mode. The magnitude of the mode bias component, however,

decreases as FA increases. As a function of mode itself the mode bias component decreases as the mode of $\mathbf{D}_\mathrm{T}$ approaches the middle of the mode scale (zero). In summary, tensors with low to intermediate values of FA (<0.70) and high extreme values of mode (>0.80 or <-0.80) tend to exhibit a bias toward higher FA values and less extreme mode values.

It is important to note that the 95%-CI contours in Fig. 6.2A demonstrate substantial overlap. This indicates that there is a low probability that two overlapping distributions are significantly different from one another. Note also, that for low FA the forward propagation of noise results in nearly any tensor mode value and even at high FA ($=0.70$) nearly half the range of mode is statistically likely. The 95%-CIs are increasingly elongated along the increasing FA-axis, which indicates a broader possible range of eigenvalues, but because of the non-linear scaling to FA this maps to a diminishingly small range of FA.

Importantly, for the 25–30+5 encoding scheme (Fig. 6.2B) the biases are quite small and the sampled 95%-CI contours are non-overlapping across the complete space of FA and mode for the selected $\mathbf{D}_\mathrm{T}$. This indicates that for this encoding scheme FA can be statistically distinguished in the presence of noise in increments of 0.15. However, it is difficult to distinguish mode at low FA ($=0.17$), but mode can be distinguished in increments of 0.3 at higher FA ($=0.70$).

Effect of $\mathrm{N_{Dir}}$. The effect of $\mathrm{N_{Dir}}$ alone in the Forward Problem is demonstrated in Figs. 6.2B and 6.2C. In summary, the effect of decreasing $\mathrm{N_{Dir}}$ while keeping SNR=25 is very similar to the effect of decreasing the SNR, whilst keeping the $\mathrm{N_{Dir}}$ constant. This is clear when comparing Figs. 6.2A and 6.2C.

Effect of K_1. The effect of different tensor trace values while keeping the 25–30+5 encoding scheme in the Forward Problem is demonstrated in Fig. 6.3. The effect of decreasing tensor trace from 2.1 to 0.6 $\mu\mathrm{m}^2/\mathrm{ms}$ (Figs. 6.3A and 6.3B)

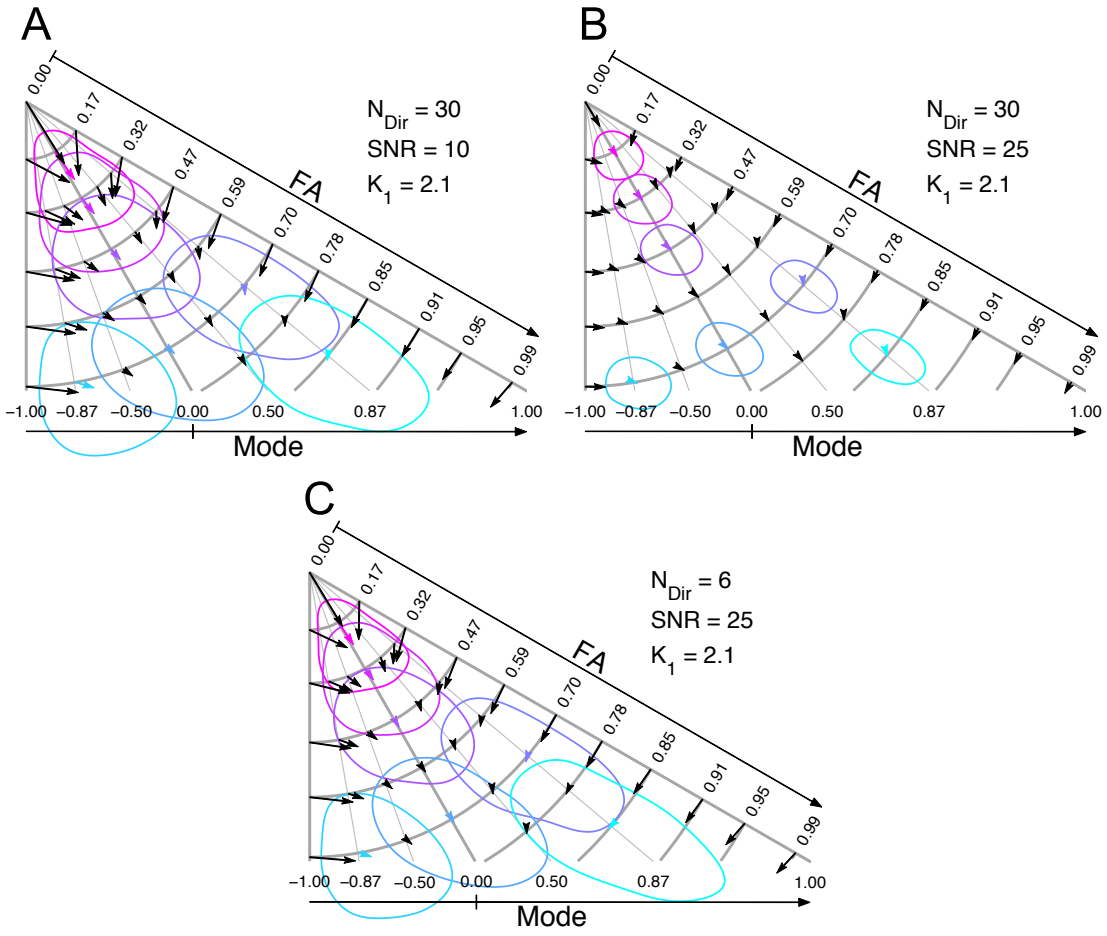

Figure 6.2: Statistics of FA and tensor mode in the Forward Problem for different encoding schemes. The biases and 95% confidence intervals of noisy FA and tensor mode over a range of FA and tensor mode with tensor trace (K_1) fixed at 2.1 μm^2/ms are shown for different encoding schemes: (A) 10–30+5, (B) 25–30+5, and (C) 25–6+1.

is similar to the effect of decreasing SNR while keeping N_{Dir}=30 (Figs. 6.2A and 6.2B), or the effect of decreasing N_{Dir} while keeping SNR=25 (Figs. 6.2B and 6.2C). When increasing tensor trace from 2.1 to 7.2 μm^2/ms (Figs. 6.3B and 6.3C), the magnitude of the bias is significantly increased, especially for $\mathbf{D}_T$ with high FA, and the bias at FA points toward much lower FA.

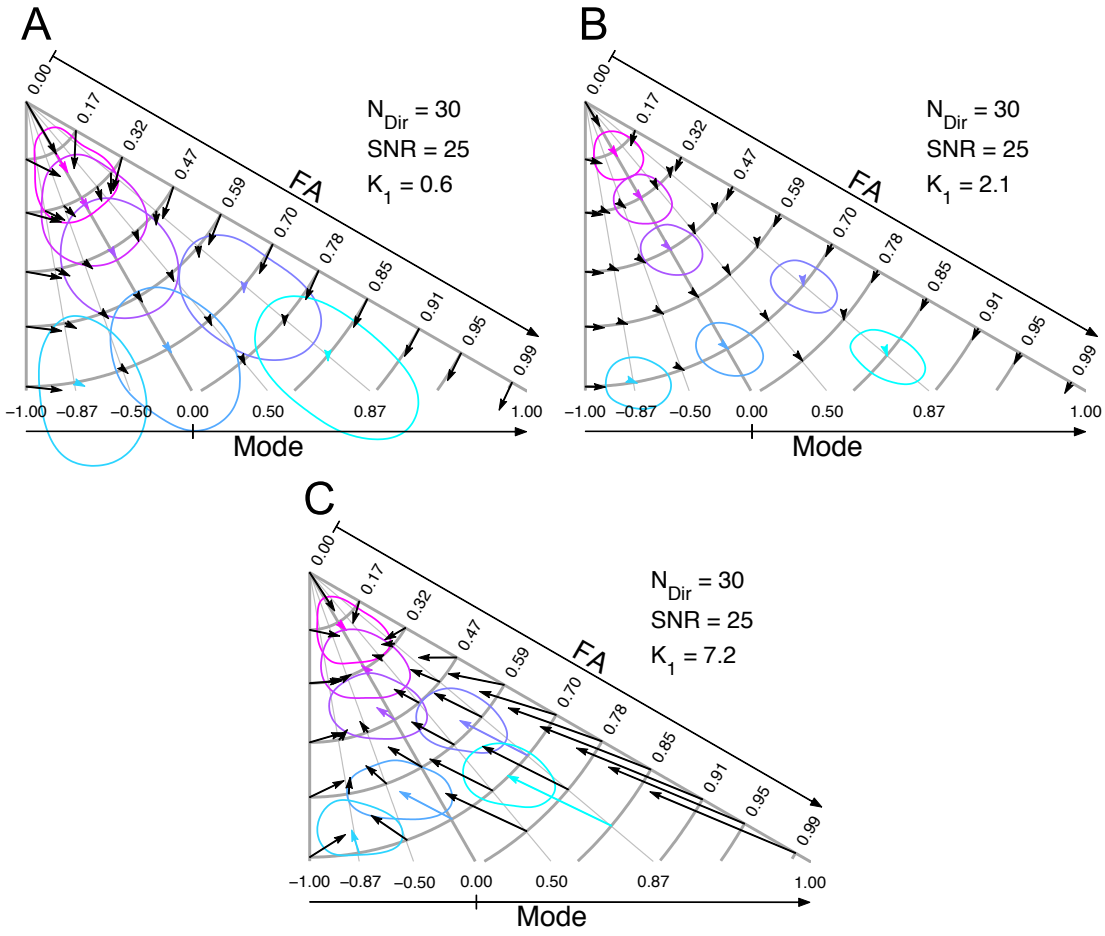

Figure 6.3: Statistics of FA and tensor mode in the Forward Problem for different tensor trace values. The biases and 95% confidence intervals of noisy FA and tensor mode over a range of FA and tensor mode with tensor trace fixed at one value (A) $K_1 = 0.6$, (B) $K_1 = 2.1$, and (C) $K_1 = 7.2$ μm^2/ms are shown for the same 25–30+5 encoding scheme.

Effect on K_1. The effect of SNR, encoding schemes, and FA and mode ranges on tensor trace alone in the Forward Problem is demonstrated in Table 6.1. The biases are quite small and the 95%-CIs are similar across the complete range of FA and mode for any encoding scheme. Decreasing SNR while keeping N_{Dir}, or reducing N_{Dir} while keeping SNR similarly increases the 95%-CIs.

The effect of different tensor trace values on tensor trace itself while keeping

FA	Mode	Encoding scheme ($K_1 = 2.1$)		
		N_{Dir}=30 SNR=10	N_{Dir}=30 SNR=25	N_{Dir}=6 SNR=25
0.17	0.00	2.10 ± 0.35	2.10 ± 0.14	2.10 ± 0.31
0.32	0.00	2.10 ± 0.36	2.10 ± 0.14	2.10 ± 0.32
0.47	0.00	2.10 ± 0.36	2.10 ± 0.14	2.10 ± 0.31
0.70	0.87	2.10 ± 0.37	2.10 ± 0.15	2.10 ± 0.33
0.70	0.00	2.10 ± 0.37	2.10 ± 0.14	2.10 ± 0.33
0.70	-0.87	2.10 ± 0.37	2.10 ± 0.15	2.10 ± 0.33
0.85	0.87	2.09 ± 0.39	2.10 ± 0.15	2.10 ± 0.35

Table 6.1: Statistics of tensor trace in the Forward Problem for different encoding schemes. The means ± two times standard deviations (95% confidence intervals) of noisy tensor trace over a range of FA and tensor mode with tensor trace (K_1) fixed at 2.1 μm^2/ms are shown for different encoding schemes: (A) 10–30+5, (B) 25–30+5, and (C) 25–6+1.

the 25–30+5 encoding scheme is demonstrated in Table 6.2. There are small biases and similar 95%-CIs across the complete range of FA and mode for a very low tensor trace value. However, there are significant biases toward lower tensor trace and larger 95%-CIs for a very high tensor trace value.

6.3.2 Effect of Noise in the Inverse Problem

The results of the Inverse Problem are novel and especially important because they provide guidance for the interpretation of measured invariants obtained from DT-MRI experiments.

FA	Mode	Tensor trace		
		$K_1 = 0.6$	$K_1 = 2.1$	$K_1 = 7.2$
0.17	0.00	0.60 ± 0.12	2.10 ± 0.14	7.14 ± 0.52
0.32	0.00	0.60 ± 0.12	2.10 ± 0.14	7.07 ± 0.52
0.47	0.00	0.60 ± 0.12	2.10 ± 0.14	6.94 ± 0.51
0.70	0.87	0.60 ± 0.12	2.10 ± 0.15	6.50 ± 0.49
0.70	0.00	0.60 ± 0.12	2.10 ± 0.14	6.57 ± 0.51
0.70	-0.87	0.60 ± 0.12	2.10 ± 0.15	6.65 ± 0.54
0.85	0.87	0.60 ± 0.12	2.10 ± 0.15	6.06 ± 0.48

Table 6.2: Statistics of tensor trace in the Forward Problem for different tensor trace values. The means ± two times standard deviations (95% confidence intervals) of noisy tensor trace over a range of FA and tensor mode with tensor trace (K_1) fixed at one value in $[0.6, 2.1, 7.2]$ μm^2/ms are shown for the same 25–30+5 encoding scheme.

Effect of SNR. The effect of noise alone in the Inverse Problem is demonstrated in Figs. 6.4A and 6.4B. For the 10–30+5 encoding scheme, the magnitude of the bias is substantially larger than for the 25–30+5 encoding scheme. Note that noise in the Inverse Problem results in a bias toward lower FA independent of FA and mode. Therefore, when observing noisy data there is a statistical bias that the observed results arose from a $\mathbf{D}_\mathrm{T}$ with a lower FA than the measured data reports. This bias, however, is essentially negligible for the 25–30+5 encoding scheme (Fig. 6.4B).

The effect of noise on tensor mode at low FA or extreme mode values near the FA and mode boundaries is very similar to the Forward Problem. At non-boundary FA and mode values, however, the bias points toward more extreme mode independent of FA and mode. Therefore, there is a statistical bias that

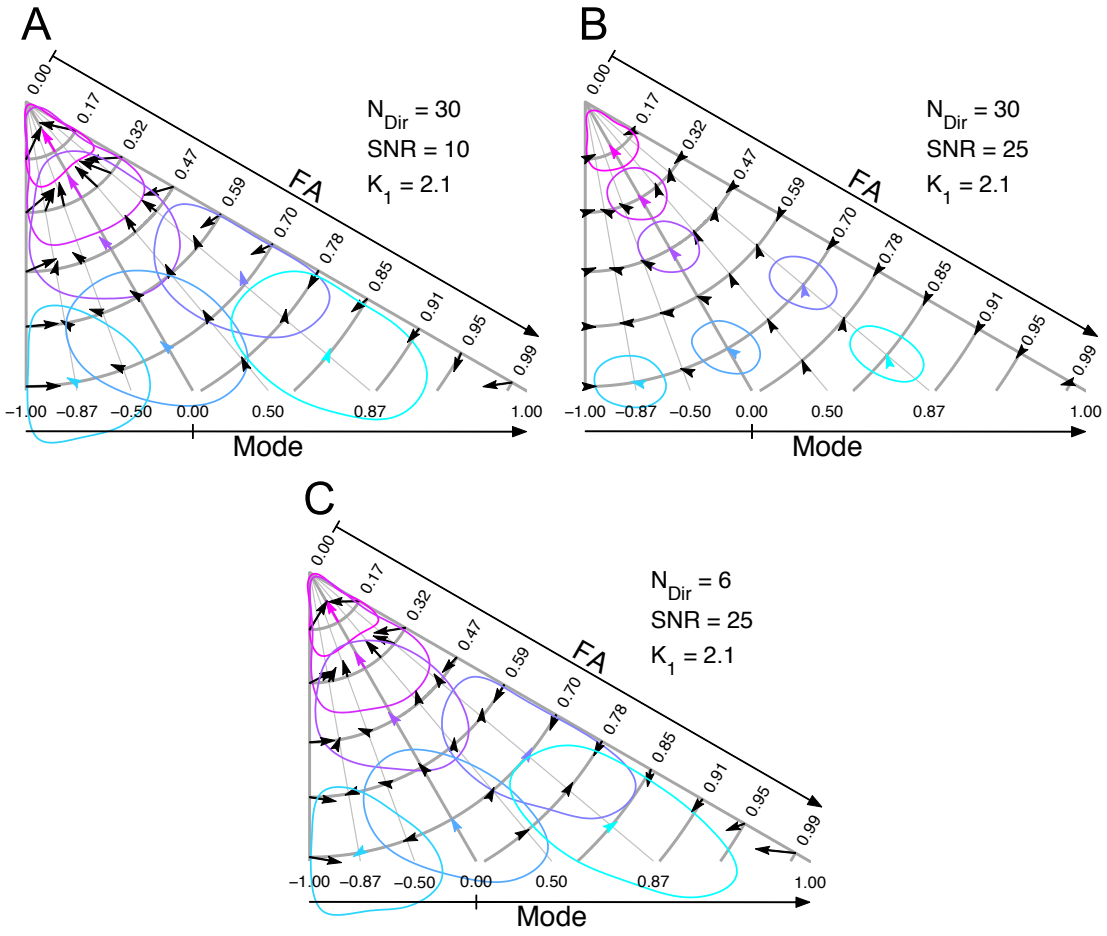

Figure 6.4: Statistics of FA and tensor mode in the Inverse Problem for different encoding schemes. The biases and 95% confidence intervals of true FA and tensor mode over a range of FA and tensor mode with tensor trace (K_1) fixed at 2.1 μm^2/ms are shown for different encoding schemes: (A) 10–30+5, (B) 25–30+5, and (C) 25–6+1.

the observed noisy tensor invariants came from a $\mathbf{D}_\mathrm{T}$ with a more extreme mode than the measured data reports. This bias is negligible for the 25–30+5 encoding scheme (Fig. 6.4B), but the 95%-CIs in mode at low FA ($\leq$0.47) are non-negligible and are approximately $\pm$0.5.

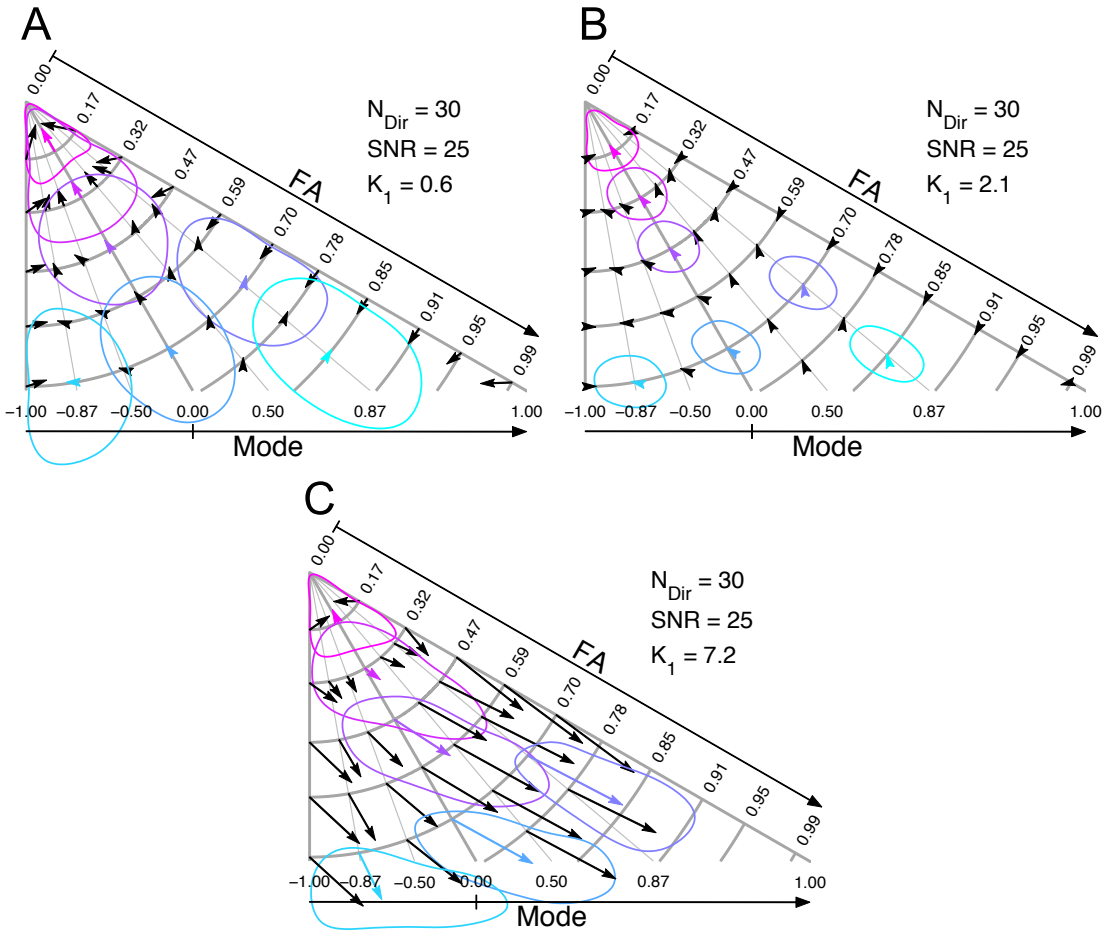

Figure 6.5: Statistics of FA and tensor mode in the Inverse Problem for different tensor trace values. The biases and 95% confidence intervals of true FA and tensor mode with tensor trace fixed at one value (A) $K_1 = 0.6$, (B) $K_1 = 2.1$, and (C) $K_1 = 7.2$ μm^2/ms are shown for the same 25–30+5 encoding scheme.

Effect of N_{Dir}. The effect of N_{Dir} alone in the Inverse Problem is demonstrated in Figs. 6.4B and 6.4C. In summary, the effect of decreasing N_{Dir} while keeping SNR=25 is very similar to the effect of decreasing the SNR, whilst keeping the N_{Dir} constant. This is clear when comparing Figs. 6.4A and 6.4C.

Effect of K_1. The effect of different tensor trace values while keeping the 25–30+5 encoding scheme in the Inverse Problem is demonstrated in Fig. 6.5. The

FA	Mode	Encoding scheme ($K_1 = 2.1$)		
		N_{Dir}=30 SNR=10	N_{Dir}=30 SNR=25	N_{Dir}=6 SNR=25
0.17	0.00	2.09 ± 0.35	2.10 ± 0.14	2.10 ± 0.31
0.32	0.00	2.11 ± 0.35	2.10 ± 0.14	2.10 ± 0.31
0.47	0.00	2.11 ± 0.35	2.10 ± 0.14	2.11 ± 0.31
0.70	0.87	2.11 ± 0.36	2.10 ± 0.15	2.11 ± 0.33
0.70	0.00	2.11 ± 0.36	2.10 ± 0.15	2.11 ± 0.32
0.70	-0.87	2.12 ± 0.36	2.10 ± 0.15	2.12 ± 0.32
0.85	0.87	2.11 ± 0.38	2.10 ± 0.15	2.10 ± 0.34

Table 6.3: Statistics of tensor trace in the Inverse Problem for different encoding schemes. The means ± two times standard deviations (95% confidence intervals) of true tensor trace over a range of FA and tensor mode with tensor trace (K_1) fixed at 2.1 μm^2/ms are shown for different encoding schemes: (A) 10–30+5, (B) 25–30+5, and (C) 25–6+1.

effect of decreasing tensor trace from 2.1 to 0.6 μm^2/ms (Figs. 6.5A and 6.5B) is similar to the effect of decreasing SNR while keeping N_{Dir}=30 (Figs. 6.4A and 6.4B), or the effect of decreasing N_{Dir} while keeping SNR=25 (Figs. 6.4B and 6.4C). When increasing tensor trace from 2.1 to 7.2 μm^2/ms (Figs. 6.5B and 6.5C), note that the magnitude of the bias is significantly increased, and the bias at FA>0.32 points toward much higher FA. Therefore, there is a significant statistical likelihood that true FA will be much higher than observed FA.

Effect on K_1. The effect of SNR, encoding schemes, and FA and mode ranges on tensor trace alone in the Inverse Problem is demonstrated in Table 6.3. The biases are quite small and the 95%-CIs are similar across the complete range of

FA	Mode	Tensor trace		
		$K_1 = 0.6$	$K_1 = 2.1$	$K_1 = 7.2$
0.17	0.00	0.59 ± 0.12	2.10 ± 0.14	7.39 ± 0.65
0.32	0.00	0.60 ± 0.12	2.10 ± 0.14	7.63 ± 1.00
0.47	0.00	0.60 ± 0.12	2.10 ± 0.14	8.01 ± 1.27
0.70	0.87	0.60 ± 0.12	2.10 ± 0.14	8.27 ± 1.35
0.70	0.00	0.60 ± 0.12	2.10 ± 0.14	8.37 ± 1.32
0.70	-0.87	0.60 ± 0.12	2.10 ± 0.14	8.59 ± 1.14
0.85	0.87	0.60 ± 0.12	2.10 ± 0.16	8.62 ± 1.05

Table 6.4: Statistics of tensor trace in the Inverse Problem for different tensor trace values. The means $\pm$ two times standard deviations (95% confidence intervals) of true tensor trace over a range of FA and tensor mode with tensor trace (K_1) fixed at one value in $[0.6, 2.1, 7.2]$ μm^2/ms are shown for the same 25–30+5 encoding scheme.

FA and mode for any encoding scheme. Decreasing SNR while keeping N_{Dir}, or reducing N_{Dir} while keeping SNR similarly increases the 95%-CIs.

The effect of different tensor trace values on tensor trace itself while keeping the 25–30+5 encoding scheme is demonstrated in Table 6.4. There are small biases and similar 95%-CIs across the complete range of FA and mode for a very low tensor trace value. However, there are significant biases toward higher tensor trace and large 95%-CIs for a very high tensor trace value.

6.4 Forward Problem Versus Inverse Problem

The paired results of the Forward Problem and the Inverse Problem over the complete space of tensor shape are shown in Figs. 6.2 and 6.4, Figs. 6.3 and 6.5,

Tables 6.1 and 6.3, and Tables 6.2 and 6.4. The bias in FA for the two problems has a naturally inverse relationship. For example, the bias points toward higher FA in Fig. 6.2A while the bias points toward lower FA in Fig. 6.4A.

The mode bias also has an inverse relationship between the Forward and Inverse Problems especially in non-boundary regions of FA and mode. At FA=0.47 and mode=−0.50, for example, the bias points toward higher mode in Fig. 6.2A while the bias points toward lower mode in Fig. 6.4A. However, the bias points toward less extreme mode in boundary regions for both problems.

6.5 Discussion

This analysis method and the mathematics developed herein define a useful framework for comparing different DT-MRI encoding schemes. Under the constraint of short exam duration and a required resolution [Zhan et al., 2013], this framework can be used to define the encoding scheme that provides the best sensitivity for measuring a tensor with any tensor shape, not limited to cylindrically symmetric anisotropic shapes. Furthermore, the Inverse Problem framework provides *direct* guidance about the confidence the observer should have in the observed measures for the encoding scheme and noise level.

This paper addresses, for example, the likelihood that a particular observation (measurement) of FA has come from underlying tissue with a lower FA. For the best encoding scheme (25–30+5), this FA bias is negligible and FA can be moderately distinguished, in increments of about 0.15. Therefore, if you want to detect a 0.15 change in FA, then this framework lets you design the appropriate experiment (e.g. 25-30+5).

If tensor mode is measured in non-boundary regions of FA, then mode is more likely to have come from underlying tissue with a more extreme mode. Strict lower and upper boundaries of 1 and 1 for mode do not allow a diffusion tensor to fall out

of the boundaries even, for example, in the presence of noise. Instead the tensor is "mirrored" to the same diffusion tensor within the boundaries by resorting the eigenvalues in descending order. Consequently, a tensor mode measured near the boundaries is more likely to arise from a less extreme mode.

For the best encoding scheme (25–30+5), this tensor mode bias is negligible if FA is sufficiently large (>0.17). Tensor mode, however, is poorly distinguished in increments of about 0.5 at FA=0.47. Therefore, we should be careful in interpreting different observations of tensor mode.

Tensor trace has no bias and a small variance for the best encoding scheme (25–30+5), and the errors are uniform across the complete space of FA and tensor mode. For both decreased and increased tensor trace values, however, the noise sensitivity is relatively higher. We performed all the simulations with the fixed b-value of 1000 s/mm^2, which attenuates the simulated DW signals by 18%, 50%, and 91%, for example, when using isotropic tensors with the apparent diffusion coefficient (ADC) values of 0.2, 0.7, and 2.4 μm^2/ms, respectively. Slow diffusion with an ADC value of 0.2 μm^2/ms does not significantly attenuate the DW signals, and therefore hampers accurate estimation of the diffusion coefficients.

The signal for fast diffusion, for example, with an ADC value of 2.4 μm^2/ms is excessively attenuated for the b-value of 1000 s/mm^2. Therefore, for an anisotropic tensor when the gradient directions are closely aligned with the primary direction of the tensor, the tensor estimation is especially sensitive to noise, which overwhelms the inherent anisotropy and the bias points towards much lower FA (Fig. 6.3C). Similarly, for highly anisotropic structures with high ADC the diffusion measurements demonstrate a bias towards decreased ADC, which also arises from an underestimate of the fast diffusion components due to noise and has a larger impact, for example, on mode=0.87 structures than mode=−0.87 structures at FA=0.7 (Table 6.2). Therefore, the optimal b-value, alternately the optimal b×ADC value, should be carefully chosen according to the range of ADC values

of the target tissues [Jones et al., 1999].

Note that our results can also provide quantitative estimates of variance. A careful comparison of our results (Figs. 6.2A and 6.2B, and Table 6.1) to the results of Chang et al. [Chang et al., 2007] (Figs. 1a and 1d) demonstrates very good agreement. For example, our estimates of the standard deviation of tensor trace and the coefficient of variation of FA for similar tensor shapes are very similar to those reported. Our results also expand on their work for tensors with mode=1 by highlighting the different response for tensors with, for example, mode=1. It is clear that the biases and 95%-CIs of trace and FA are similar for both tensor shapes, but the tensor mode bias is oppositely directed.

Note that the number of gradient directions is not necessarily the same as the number of acquisitions. Figures 6.2A and 6.2C, for example, compare a large number of gradient directions (N_{Dir}=30) with moderate SNR=10 to a low number of gradient directions (N_{Dir}=6) and high SNR=25. If the imaging system is fixed, and it takes 1 minute to acquire a single non-diffusion weighted image with SNR=10, then it will require 6.25-minute per image to achieve SNR=25 by averaging. Hence, 30 1-minute acquisitions have a roughly equivalent acquisition time compared to a 37.5 (6×6.25)-minute acquisition and we may expect similar impacts on the distribution of noisy tensors. Also note that while noise is an important source of variability that impacts tensor estimation, physiologic and patient motion, eddy currents, B1-inhomogeneity, multi-coil acquisitions and the partial volume effects of fat should also be considered.

CHAPTER 7

Uniform Tensor Invariant Set

7.1 Introduction

Diffusion tensor MRI (DT-MRI) characterizes the microstructural features of soft biological tissues by measuring the self-diffusion rate of water molecules within the tissues [Basser et al., 1994a]. Tensor invariants have been commonly used to characterize the salient and geometric features of the microstructural shape. Tensor invariants can be categorized into the three components of tensor shape: the magnitude-of-isotropy (trace, norm, determinant), magnitude-of-anisotropy (fractional anisotropy, relative anisotropy) and kind-of-anisotropy (skewness, mode). Trace (three times mean diffusivity) and fractional anisotropy (FA) are amongst the most widely used for the clinical analysis of diffusion tensor fields [Sotak, 2002, Thomalla et al., 2004]. Mode is an emerging tensor invariant that characterizes another component of tensor shape (planar-orthotropic-linear anisotropy) and completes the description of tensor shape [Jolapara et al., 2009].

Though mathematically convenient, however, It is not fully studied if these invariants are truly logical and reliable to characterize tensor shape and quantify a change in tensor shape. Tensor shapes and their changes are intuitively investigated by visualizing tensors with ellipsoidal or superqardric glyphs whose axial lengths are usually set the eigenvalues [Ennis et al., 2005]. Hence it is desirable that evenly spaced values of an invariant produce uniform changes of visualized shapes which are equivalent to uniform distances between the eigenvalues for each

step.

Comparative studies between FA and other anisotropy measures including relative anisotropy (RA) mostly consider the contrast-to-noise ratio (CNR) or signal-to-noise ratio (SNR) [Papadakis et al., 1999, Sorensen et al., 1999, Alexander et al., 2000, Hasan et al., 2004]. FA is widely accepted to have better noise immunity and preferred in the literature for characterizing tensor anisotropy. A more recent study, on the other hand, showed that FA has been preferred due to the popularity and has no remarkable advantage in the CNRs [Kingsley and Monahan, 2005, Kingsley, 2006]. The authors also claimed that RA is more logical because evenly spaced values of RA accord to evenly spaced largest eigenvalues for cylindrically symmetric tensors (mode of +1, the smaller eigenvalues are the same). Extensive studies over a wide range of tensor shape, however, are needed to bolster the claim.

This paper proposes the *uniform invariant* set consisting of trace, RA and *angular mode* (the arccos of mode, AM) that more logically (linearly) characterizes the complete space of tensor shape. It is mathematically shown that evenly spaced values of each invariant in the set produce uniform distances between the eigenvalues for each step exclusively (other invariants are fixed arbitrary values). The logical property of the uniform invariant set is demonstrated by comparison to FA and mode for tensor field interpolation and analysis of experimentally measured cardiac diffusion tensor fields.

7.2 Theory

Our uniform tensor invariant set (U_i) consists of tensor trace (U_1), scaled RA (U_2) and scaled AM (U_3) and is defined for a tensor $\mathbf{D}$:

$$\begin{aligned} U_1 &= \mathrm{tr}\mathbf{D} \\ U_2 &= \sqrt{\frac{3}{2}}\frac{\mathrm{norm}\widetilde{\mathbf{D}}}{\mathrm{tr}\mathbf{D}} \\ U_3 &= 1 - \frac{2}{\pi}\arccos R_3(\mathbf{D}) \ , \end{aligned} \tag{7.1}$$

where $\widetilde{\mathbf{D}} = \mathbf{D} - (\mathrm{tr}\mathbf{D})\,\mathbf{I}/3$, $R_3(\mathbf{D}) = \mathrm{mode}\mathbf{D} = 3\sqrt{6}\mathrm{det}\widetilde{\mathbf{D}}/(\mathrm{norm}\widetilde{\mathbf{D}})^3$, and tr, norm and det are the tensor trace, Frobenius norm and determinant, respectively. The original RA [Basser, 1995] was scaled to range from 0 (isotropic) to 1 (anisotropic) [Kingsley and Monahan, 2005]. Scaled RA (U_2) can be expressed as a function of FA (R_2):

$$U_2 = \frac{R_2}{\sqrt{3 - 2R_2^2}} \ , \tag{7.2}$$

and their relationship is plotted in Fig. 7.1a. Whereas R_2 increases from 0 to 1 at a constant rate, U_2 starts slowly, monotonically increases at an increasing rate and ends rapidly. AM is the arccos of mode (R_3) [Bahn, 1999], and also scaled to be between -1 (planar), 0 (orthotropic) and $+1$ (linear) as mode, which will be named *scaled AM* (U_3). The relationship between R_3 and U_3 is plotted in Fig. 7.1b. They meet at -1, 0 and $+1$, and when R_3 increases from 0 to $+1$ or decreases from 0 to -1 at a constant rate, U_3 starts slowly, the magnitude increases at an increasing rate and U_3 approaches $+1$ or -1 rapidly.

We prove in the following that uniformly spaced values of each U_i produce uniform distances between the eigenvalues for each step when other invariants are arbitrarily fixed.

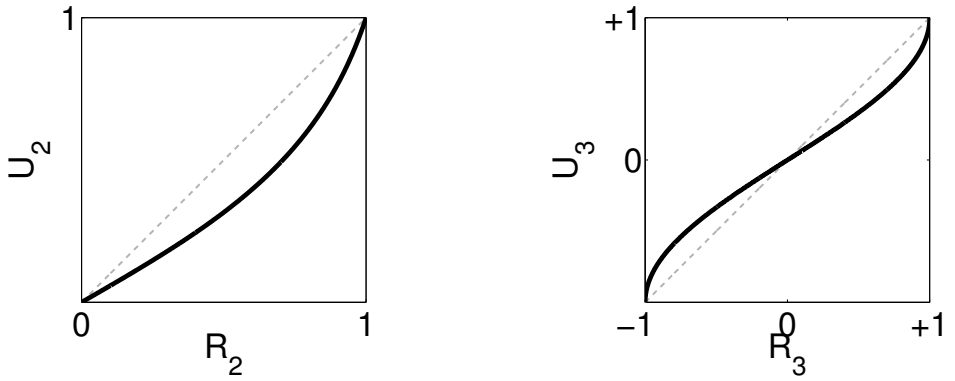

(a) R_2 vs. U_2 (b) R_3 vs. U_3

Figure 7.1: Relationship between a) FA (R_2) and scaled RA (U_2) and b) mode (R_3) and scaled angular mode (U_3).

7.2.1 Uniformity of RA

The mathematics that defines how eigenvalues (λ_i, sorted in decreasing order) can be computed from the tensor invariant set composed of trace, FA and mode was recently established as shown in Eq. 2.23. This can be rewritten using the uniform invariant set U_i defined in Eq. 7.1:

$$\begin{aligned}
\lambda_1 &= \tfrac{1}{3}U_1 - \tfrac{2}{3}U_1U_2\sin(\tfrac{\pi}{6}U_3 - \tfrac{2\pi}{3}) \\
\lambda_2 &= \tfrac{1}{3}U_1 - \tfrac{2}{3}U_1U_2\sin(\tfrac{\pi}{6}U_3) \\
\lambda_3 &= \tfrac{1}{3}U_1 - \tfrac{2}{3}U_1U_2\sin(\tfrac{\pi}{6}U_3 + \tfrac{2\pi}{3}) \ .
\end{aligned} \tag{7.3}$$

Suppose two arbitrary tensors $\mathbf{A}$ and $\mathbf{B}$ have different values only in U_2 (U_1 and U_3 are fixed). Then the distance between the eigenvalues ($\lambda = [\lambda_1, \lambda_2, \lambda_3]$) for $\mathbf{A}$ and $\mathbf{B}$ can be expressed in terms of U_i using Eq. 7.3:

$$\begin{aligned}
\|\lambda(\mathbf{A}) - \lambda(\mathbf{B})\| &= \tfrac{2}{3}U_1|U_2(\mathbf{A}) - U_2(\mathbf{B})|\left[\sum_i \sin^2\left(\tfrac{\pi}{6}U_3 + P_i\right)\right]^{1/2} \\
&= \tfrac{\sqrt{6}}{3}U_1|U_2(\mathbf{A}) - U_2(\mathbf{B})| \ ,
\end{aligned} \tag{7.4}$$

where the reduction is easily done using trigonometric identities. The distance between the eigenvalues is proportional to the U_2 difference with the coefficient

determined by U_1 (independent of U_3). Therefore if the U_2 differences between any pair of tensors are the same then the distances of eigenvalues are also the same. This implies that evenly spaced U_2 values also produce uniform distances between the eigenvalues for each step.

Figure 7.2a demonstrates the uniformity of U_2 by visualizing the tensor shape with superquadric glyphs whose axial lengths are fixed eigenvalues. The evenly spaced values of U_2 and R_2 are chosen between $U_2 = R_2 = 0$ (isotropic) and $U_2 = R_2 = 1$ (fully anisotropic), and $U_3 = R_3 = +1$ (cylindrically symmetric) with U_1 fixed. The U_2 values generate uniform steps in the eigenvalue space, which shows a constant rate of change in the visualized shapes from the isotropic to linear shape. However, the R_2 values do not allow for the constant change. In particular there exist a slow change between the isotropic and low anisotropic parts and a rapid change between the high anisotropic and linear parts.

7.2.2 Uniformity of AM

Arbitrary tensors $\mathbf{A}$ and $\mathbf{B}$ are alternatively assumed to have different values of U_3 (U_1 and U_3 fixed). Then the distance between the eigenvalues for A and B is expressed using Eq. 7.3:

$$\begin{aligned}
&\|\lambda(\mathbf{A}) - \lambda(\mathbf{B})\| \\
&= \tfrac{2}{3}U_1U_2\left[\sum_i \left[\sin\left\{\tfrac{\pi}{6}U_3(\mathbf{A}) + P_i\right\} - \sin\left\{\tfrac{\pi}{6}U_3(\mathbf{B}) + P_i\right\}\right]^2\right]^{1/2} \\
&= \tfrac{2\sqrt{6}}{3}U_1U_2 \sin\tfrac{\pi}{12}|U_3(\mathbf{A}) - U_3(\mathbf{B})| \ , \qquad (7.5)
\end{aligned}$$

where the reduction is also carried out using trigonometric identities. The distance between the eigenvalues is the sine function of the U_3 difference with the coefficient proportional U_1U_2 (constant). Therefore evenly spaced values of U_3 also guarantee uniform distances between the eigenvalues for any pair of the adjacent U_3 values.

An example of the U_3 uniformity is shown in Fig. 7.2b. The evenly spaced

values of U_3 and R_3 are chosen between $U_3 = R_3 = 0$ (orthotropic) and $U_3 = R_3 = +1$ (linear), and $U_2 = 0.57 \Leftrightarrow R_2 = 0.77$ (anisotropic) and U_1 are fixed. The U_3 values generate uniform steps in the eigenvalue space, which shows a constant rate of change in the visualized shapes from the orthotropic to linear shape. Figure 7.2b also shows that the R_3 values fail to generate uniform distances of eigenvalues between any consecutive steps. There exist a slow change at low U_3 or R_3 and a rapid change at high U_3 or R_3.

The uniformity of tensor trace (U_1) can be similarly proven. The distance between the eigenvalues is given, when U_2 and U_3 are fixed:

$$\|\lambda(\mathbf{A}) - \lambda(\mathbf{B})\| = \sqrt{(1 + 2U_2^2)/3}\,|U_1(\mathbf{A}) - U_1(\mathbf{B})| \ . \tag{7.6}$$

7.3 Methods

The mathematical motivation for U_i was shown above. The uniform invariant set is more logical for representing tensor shape and characterizing its change than the conventional invariant set. The uniform invariant set can be used for any tensor invariant-based processing and analysis of diffusion tensor fields. It will be shown, in particular, that scaled RA (U_2) and scaled AM (U_3) are better in practice for recovering the microstructural features in tensor interpolation and examine miscrostructural remodeling by disease using cardiac diffusion tensor fields.

7.3.1 Linear Interpolation of U_i

Linear interpolation of trace, FA and mode was recently proposed in order to preserve the microstructural features characterized by the invariants [Gahm et al., 2012]. The linear invariant (LI) interpolation method resolved the underestimation of FA (R_2) inherent to the Riemannian approaches including log-Euclidean (LE) [Arsigny et al., 2006], but underestimated mode (R_3). Geodesic-loxodrome

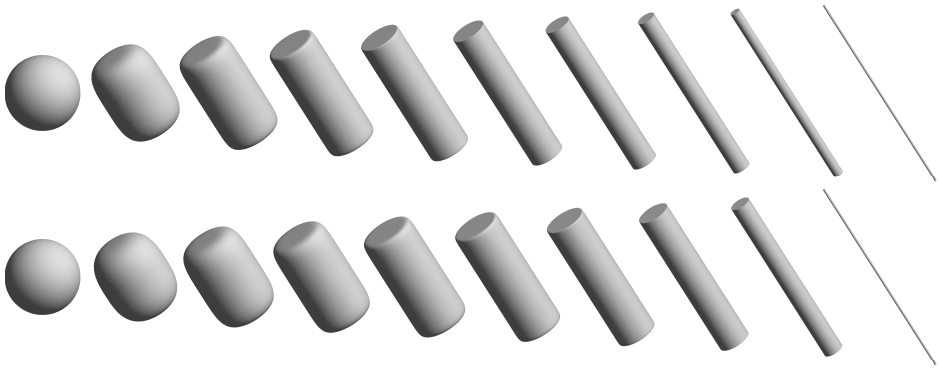

(a) U_2 (top) vs. R_2 (bottom)

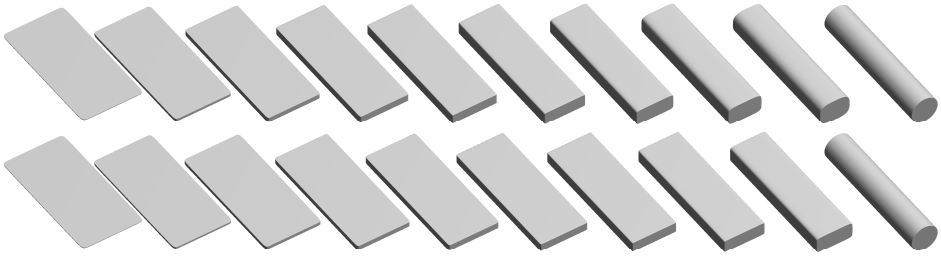

(b) U_3 (top) vs. R_3 (bottom)

Figure 7.2: Visualization of tensors generated by evenly spaced values of a) U_2 and R_2 between 0 and 1 and b) U_3 and R_3 between 0 and +1 (between the same end tensors for U_i and R_i). U_i shows more plausible (uniform) changes in visualized tensor shape.

(GL) [Kindlmann et al., 2007b] was reported to most accurately recover all the invariants including R_3, but not practical due to the significant computational time. Instead linear interpolation of the U_i set is herein proposed, which will be termed *linear uniform-invariant (LU)* interpolation. Each invariant in the set is separately interpolated in a linear manner and then the interpolated invariants are easily converted into the eigenvalues using Eq. 7.3. LU was evaluated with comparison to LE, GL and LU using the three real DT-MRI datasets measured from rabbit, pig and human hearts same as used in Chapter 3. The data was downsampled and recovered using each interpolation method, and the 95% bootstrapped confidence interval (CI) of the bias rates (differences normalized by median) was

computed for each invariant as described in Section 3.3.

7.3.2 Microstructural Remodeling

There are several recent studies of microstructural remodeling in infarcted myocardium using tensor invariants including FA (R_2) [Kung et al., 2012, Wu et al., 2011, Strijkers et al., 2009]. The distinct differences in R_2 (and R_3) between remote, peri-infarct and infarct regions were reported. Studies that use R_2 and R_3, however, may be misleading into wrong interpretation of each distribution and comparison between the distributions. Instead U_2 and U_3 more logically quantify the magnitude-of-anisotropy and kind-of-anisotropy. Therefore their distributions and comparisons better accord with visual interpretation and the reparameterization results in large apparent differences in the histogram, which may infer U_i is more sensitive to changes in microstructure. U_2 and U_3 distributions were compared to R_2 and R_3 distributions for remote, peri-infarct and infarct regions using a real DT-MRI dataset measured from the post-infarct pig heart.

7.4 Results

Figure 7.3 shows the 95% bootstrapped CIs of the bias rates using each interpolation method for recovery of R_i and U_i using the three experimentally measured DT-MRI datasets. Both LI and LU have no significant bias (rabbit and pig) or the least bias (human) for recovery of R_2 and U_2. LU introduces significantly less bias for recovery of R_3 than LI but still slightly underestimated R_3 (pig and human). For recovery of U_3, however LU has no significant bias for all the datasets. Furthermore GL positively biases U_3 and LE's bias is significantly increased ($\approx 10\%$ bias rate) compared to R_3.

Figure 7.4 shows the bootstrapped histograms with 95% CIs of R_i and U_i for remote, peri-infarct and infarct regions in the post-infarct pig heart. There exists

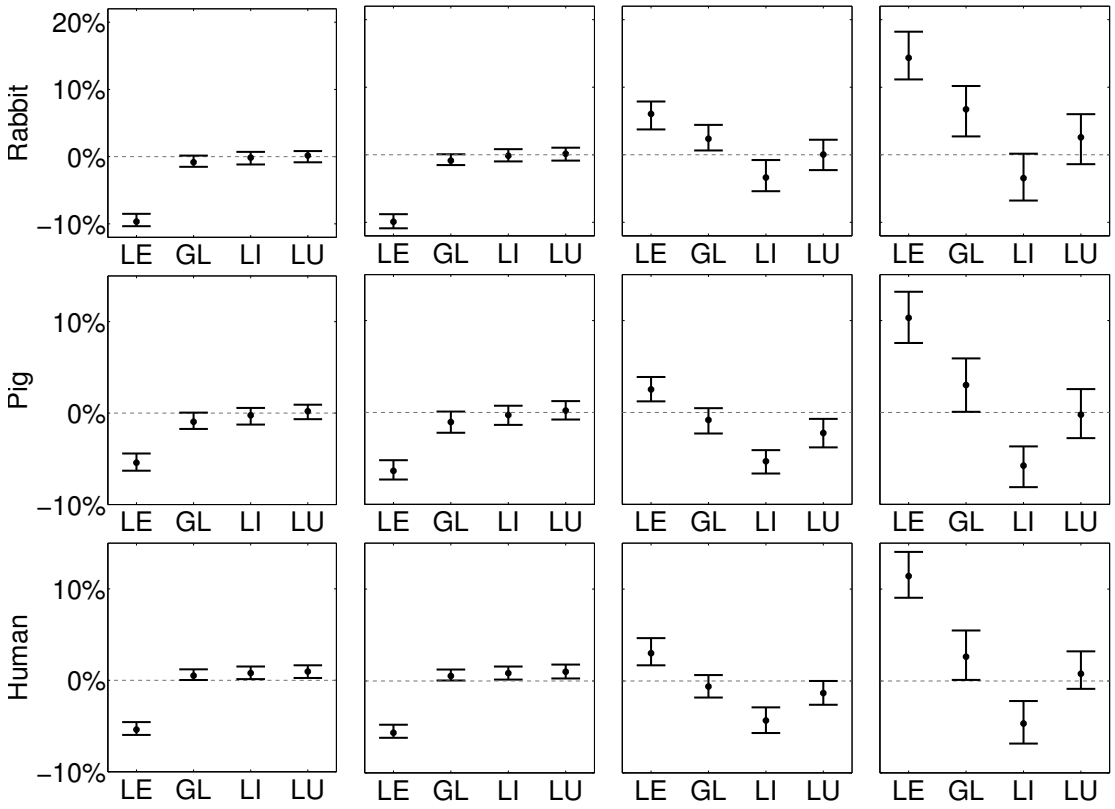

(a) R_2 (b) U_2 (c) R_3 (d) U_3

Figure 7.3: Bootstrapped results of tensor interpolation using the real data. Each bar represents the 95% confidence interval of the bias rates about the median. LU introduces significantly less bias both in R_3 and U_3 than LU and no bias in U_3.

a distinct decrease both in R_2 and U_2 from remote to infarct regions, but the U_2 distributions are narrower and less shifted between remote and infarct regions within the lower half range of U_2. The difference between R_3 and U_3 is more obvious. Any shift in the R_3 distributions is difficult to observe and measure, but the U_3 distributions are more bell-shaped and slightly left-shifted from remote to infarct regions. The U_3 histogram is also more consistent with the qualitative observation of a median tensor shape that is orthotropic.

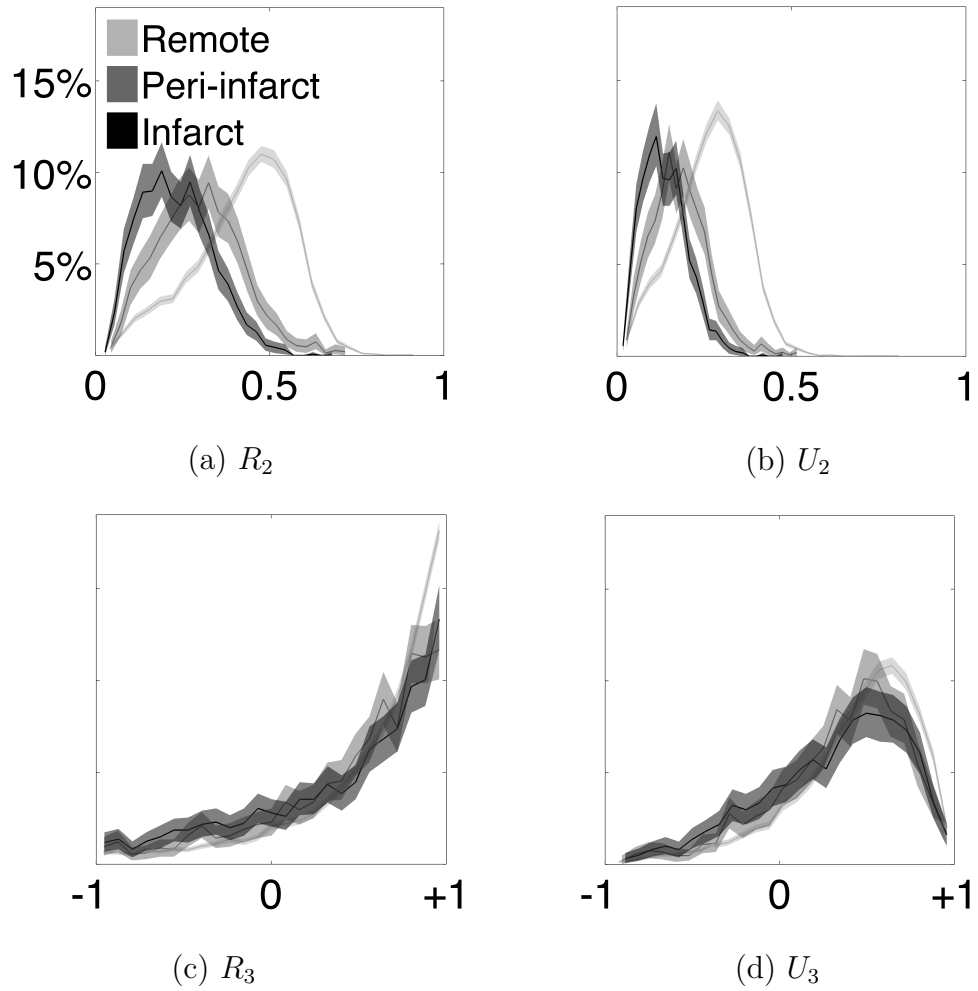

(a) R_2 (b) U_2

(c) R_3 (d) U_3

Figure 7.4: Bootstrapped histograms of each invariant for remote, peri-infarct and infarct regions in the infarct heart. U_2 is more narrowly distributed than R_2 but with distinction between regions. Unlike R_3, the U_3 distributions are bell-shaped and distinct between regions.

7.5 Discussion

Measurements of tensor anisotropy that accurately quantify a change in tensor shape are important in tensor invariant-based processing and analysis of tensor invariants altered by disease. The uniform invariant set including scaled RA and AM provides a linear relationship between each invariant in the set and tensor shape (component) characterized by the invariant. FA and mode may overem-

phasize a change in tensor shape at the low magnitude and understate at the high magnitude. The interpolation results show that linear interpolation of the uniform invariants generates more linear interpolation of tensor shape and introduces no significant bias for recovery of each component of cardiac microstructural shape. The comparison results of invariant histograms demonstrate the significant difference between using the uniform and non-uniform invariants. The histograms of the uniform invariants allow for more accurately evaluating how broadly each component of tensor shape is distributed and how the degree of the shape component is altered by disease.

Note that each uniform invariant exclusively satisfies the uniformity, but not simultaneously. Such an invariant set does not seem to exist in the eigenvalue space. We believe, however, that this does not undermine our claim. Tensor invariant-based processing or analysis including the examples presented herein independently deals with each component of tensor shape characterized by each invariant (by projecting tensors on the iso-other invariants line in the eigenvalue space). When we investigate a FA or RA map to characterize the magnitude-of-anisotropy, for example, we do not consider the magnitude-of-isotropy (trace) at the same time. Only the uniform invariant set provides a logical (linear) mapping between the shape component-invariant pair for the independent component analysis.

CHAPTER 8

Conclusion

This dissertation presented methods for tensor field processing (interpolation and segmentation) and analysis of diffusion tensor fields that preserve features of microstructural shape and orientation, are mathematically unambiguous, and computationally efficient. The microstructural feature-based processing and analysis methods were accomplished by direct tensor field processing of each component of tensor shape and orientation, and recapitulation of the tensor from the tensor components using the mathematics we developed (Section 2.4).

Tensor field processing tasks such as interpolation, segmentation and registration require an appropriate tensor metric. Various tensor metrics exist and the Riemannian approaches are amongst the most widely used in the literature. The Riemannian tensor metrics largely rose to prominence because they preserve both the tensor determinant and the positive definiteness of diffusion tensors. The LE and AI approaches were quickly adopted because they closely approximate the Riemannian metrics and are easier to compute. The Riemannian metrics were, however, not microstuctural feature-based and failed to preserve important microstructural features of shape and orientation in tensor field interpolation. The geodesic-loxodrome approach was developed that preserves microstructural features of shape by monotonically interpolating an orthogonal tensor invariant set, but was not practical due to the significant computational time. Furthermore, these tensor-based approaches mostly focused on tensor shape, and had no distinct advantage for tensor orientation interpolation.

Our microstructural feature-based approach separately processed tensor shape and orientation. The tensor shape interpolation was accomplished by linearly interpolating each component of tensor shape, and converting the interpolated invariants into the eigenvalues, so called linear uniform-invariant (LU) interpolation. The tensor orientation interpolation was done by linearly interpolating the dyadic tensors of each eigenvector with subsequent reduction to rank-1 dyadics and orthogonal matrices, so called dyadic tensor-based (DY) interpolation. LU combined with DY to create a microstructural feature-based interpolation technique was computationally efficient, commutative, and accurate based on our experimental results.

The linearity of tensor invariants was also used in tensor shape interpolation applied to define the weighted tensor distance measurement of shape and orientation components for segmentation of diffusion tensor fields. The microstructural feature-based tensor distance measurement was advantageous in segmentation of anatomical objects that commonly have high contrast between particular shape and orientation components.

The microstructural feature-based analysis, on the other hand, involved evaluating the effects of noise on characterizing tensor shape. Previous work examined the effects of noise only over a narrow range of tensor shape, and only considered the forward propagation of noise. Our work provided the statistical distributions of tensor invariants over the complete space of tensor shape. In addition, we developed a new framework termed the "Inverse Problem" for determining the distribution of the likely true values of tensor invariants given their noisy measures. This work is important for redefining our expectations for the effects of noise when we observe and analyze noisy data.

The microstructural feature-based tensor processing and analysis methods needed to choose an appropriate tensor invariant set that fully characterized tensor shape, and the set of trace, FA and mode was firstly chosen due to their

widespread use in the literature. FA and mode, however, failed to linearly characterize their shape components, that is, evenly spaced values of FA and mode did not provide equal distances between the eigenvalues for each step. The non-uniformity of mode, in particular, adversely affected the tensor shape interpolation and evaluation of microstructural remodeling because it skewed intermediate kinds-of-anisotropy to relatively high values of tensor mode. We demonstrated that scaled RA and angular mode linearly reparameterized the same tensor components characterized by FA and mode (along the same path in the eigenvalue space). The uniform tensor invariant set consisting of trace, scaled RA, and scaled angular mode introduced no bias for recovery of each component of cardiac microstructural shape and allowed for more accurate evaluation of microstructural remodeling by cardiac disease.

As a result of this work, we have:

- a tensor field interpolation method that best preserves cardiac microstructural features (Chapters 3, 4 and 7) [Gahm et al., 2012, Gahm and Ennis, 2014a,b].
- a uniform tensor invariant set that linearly characterizes tensor shape (Chapter 7) [Gahm and Ennis, 2014b].
- an evaluation of the effects of noise on characterizing tensor shape over the complete space of tensor shape (Chapter 6) [Gahm et al., 2014].
- a microstructural feature-based segmentation of cardiac diffusion tensor fields (Chapter 5) [Gahm et al., 2013].

8.1 Future Work

The uniform tensor invariant set was most recently developed and the mathematical foundation was firmly established. The uniform tensor invariant set was

applied only to the linear interpolation of tensor invariants and qualitative evaluation of tensor invariant-based microstructural remodeling. The uniform tensor invariant set can readily be used in many other micro-structural feature-based processing and analysis tasks including tensor distance measurement for segmentation of tensor fields, and evaluation of the effects of noise on tensor invariants presented herein. Future work should evaluate these applications, and focus on a quantitative evaluation of microstructural remodeling.

The tensor shape and orientation interpolation methods were evaluated using experimentally measured DT-MRI data from ex vivo hearts. Further investigations using brain DT-MRI data and the same evaluation process may be needed to evaluate if the most accurate interpolation is dependent on the underlying tissue characteristics. For tensor orientation interpolation, in particular, all the tested tensor interpolation methods except the quaternion method introduced a $\approx 5^\circ - 8^\circ$ bias for recovery of the primary fiber direction. However, the required tensor interpolation accuracy for cardiac mechanics and EP simulations remains incompletely understood. If the bias turns out to introduce notable fiber disarray, a tensor interpolation method that better recovers tensor orientation is still needed.

The development of the mathematics to freely construct tensors with known shape attributes was enabling for both the Inverse and Forward Problems in the evaluation of effects of noise. This technique was also used to devise the tensor interpolation methods and the uniform tensor invariant set. Moving forward, the mathematical framework could also be used to constrain tensor-field reconstruction; for tensor-field denoising; and for compressed sensing acquisition and reconstruction of tensor field data.

Bibliography

A. L. Alexander, K. Hasan, G. Kindlmann, D. L. Parker, and J. S. Tsuruda. A geometric analysis of diffusion tensor measurements of the human brain. *Magn Reson Med*, 44(2):283–291, 2000. 74

V. Arsigny, P. Fillard, X. Pennec, and N. Ayache. Log-Euclidean metrics for fast and simple calculus on diffusion tensors. *Magn Reson Med*, 56:411–421, 2006. 3, 18, 22, 23, 30, 31, 41, 42, 78

M. M. Bahn. Invariant and orthonormal scalar measures derived from magnetic resonance diffusion tensor imaging. *J Magn Reson*, 141:68–77, 1999. 75

R. F. Barajas, Jr, J. L. Rubenstein, J. S. Chang, J. Hwang, and S. Cha. Diffusion-weighted MR imaging derived apparent diffusion coefficient is predictive of clinical outcome in primary central nervous system lymphoma. *Am J Neuroradiol*, 31:60–66, 2010. 57

P. J. Basser. Inferring microstructural features and the physiological state of tissues from diffusion-weighted images. *NMR Biomed*, 8:333–344, 1995. 13, 75

P. J. Basser and S. Pajevic. Statistical artifacts in diffusion tensor MRI (DT-MRI) caused by background noise. *Magn Reson Med*, 44:41–50, 2000. 33, 52

P. J. Basser and C. Pierpaoli. Microstructural and physiological features of tissues elucidated by quantitative-diffusion-tensor MRI. *J Magn Reson B*, 111(3):209–219, 1996. 1

P. J. Basser, J. Mattiello, and D. LeBihan. Estimation of the effective self-diffusion tensor from the NMR spin echo. *J Magn Reson B*, 103(3):247–254, 1994a. 1, 73

P. J. Basser, J. Mattiello, and D. LeBihan. MR diffusion tensor spectroscopy and imaging. *Biophys J*, 66:259–267, 1994b. 2, 12, 52

P. G. Batchelor, M. Moakher, D. Atkinson, F. Calamante, and A. Connelly. A rigorous framework for diffusion tensor calculus. *Magn Reson Med*, 53:221–225, 2005. 3, 18

J. Blow. Understanding slerp, then not using it. *Game Developer Mag*, Apr 2004. 32

L. C. Chang, C. G. Koay, C. Pierpaoli, and P. J. Basser. Variance of estimated DTI-derived parameters via first-order perturbation methods. *Magn Reson Med*, 57:141–149, 2007. 45, 52, 53, 60, 72

J. C. Criscione, J. D. Humphrey, A. S. Douglas, and W. C. Hunter. An invariant basis for natural strain which yields orthogonal stress response terms in isotropic hyperelasticity. *J Mech Phys Solids*, 48(12):2445–2465, 2000. 13, 16

D. B. Ennis and G. Kindlmann. Orthogonal tensor invariants and the analysis of diffusion tensor magnetic resonance images. *Magn Reson Med*, 55:136–146, 2006. 2, 12, 13, 14, 31, 52

D. B. Ennis, G. Kindlmann, I. Rodriguez, P. A. Helm, and E. R. McVeigh. Visualization of tensor fields using superquadric glyphs. *Magn Reson Med*, 53: 169–176, 2005. 23, 36, 73

P. T. Fletcher and S. Joshi. Riemannian geometry for the statistical analysis of diffusion tensor data. *Signal Processing*, 87(2):250–262, 2007. 3, 18

J. K. Gahm and D. B. Ennis. Dyadic tensor-based interpolation of tensor orientation: application to cardiac DT-MRI. In *Stat Atlases and Comp Models of the Heart (STACOM), MICCAI Workshop 2013*, volume 8330 of *LNCS*, pages 135–142. Springer Berlin Heidelberg, 2014a. 6, 86

J. K. Gahm and D. B. Ennis. Uniform tensor invariant set and the application

in cardiac DT-MRI. In *Med Image Comput Comput Assist Interv (MICCAI) 2014*, 2014b. {Submitted}. 6, 7, 86

J. K. Gahm, N. Wisniewski, G. Kindlmann, G. L. Kung, W. S. Klug, A. Garfinkel, and D. B. Ennis. Linear invariant tensor interpolation applied to cardiac diffusion tensor MRI. In *Med Image Comput Comput Assist Interv (MICCAI) 2012*, volume 7511 of *LNCS*, pages 494–501. Springer Berlin Heidelberg, 2012. 6, 31, 40, 41, 42, 78, 86

J. K. Gahm, G. L. Kung, and D. B. Ennis. Weighted component-based tensor distance applied to graph-based segmentation of cardiac DT-MRI. In *Biomed Imaging (ISBI), 2013 IEEE 10th Int Symp on*, pages 504–507, 2013. 6, 86

J. K. Gahm, G. Kindlmann, and D. B. Ennis. The effects of noise over the complete space of diffusion tensor shape. *Med Image Anal*, 18:197–210, 2014. 3, 7, 16, 17, 86

K. M. Hasan, P. J. Basser, D. L. Parker, and A. L. Alexander. Analytical computation of the eigenvalues and eigenvectors in DT-MRI. *J Magn Reson*, 152: 41–47, 2001. 16

K. M. Hasan, A. L. Alexander, and P. A. Narayana. Does fractional anisotropy have better noise immunity characteristics than relative anisotropy in diffusion tensor MRI? An analytical approach. *Magn Reson Med*, 51(2):413–417, 2004. 74

Drs. Patrick A. Helm, Raimond L. Winslow at the Center for Cardiovascular Bioinformatics, Modeling, and Dr. Elliot McVeigh at the National Institute of Health for provision of data. 21

R. M. Henkelman. Measurement of signal intensities in the presence of noise in MR images. *Med Phys*, 12(2):232–233, 1985. 54

E. W. Hsu, A. L. Muzikant, S. A. Matulevicius, R. C. Penland, and C. S. Henriquez. Magnetic resonance myocardial fiber-orientation mapping with direct histological correlation. *Am J Physiol*, 274(5):H1627–H1634, 1998. 1, 2

M. Jolapara, C. Kesavadas, V. V. Radhakrishnan, J. Saini, S. N. Patro, A. K. Gupta, T. R. Kapilamoorthy, and N. Bodhey. Diffusion tensor mode in imaging of intracranial epidermoid cysts: one step ahead of fractional anisotropy. *Neuroradiology*, 51(2):123–129, 2009. 2, 14, 73

D. K. Jones. The effect of gradient sampling schemes on measures derived from diffusion tensor MRI: a Monte Carlo study. *Magn Reson Med*, 51(4):807–815, 2004. 3, 52, 53, 60

D. K. Jones, M. A. Horsfield, and A. Simmons. Optimal strategies for measuring diffusion in anisotropic systems by magnetic resonance imaging. *Magn Reson Med*, 42(3):515–525, 1999. 54, 72

G. Kindlmann, D. B. Ennis, R. T. Whitaker, and C. F. Westin. Diffusion tensor analysis with invariant gradients and rotation tangents. *IEEE Trans Med Imaging*, 26(11):1483–1499, 2007a. 2, 12, 45

G. Kindlmann, R. San José Estépar, M. Niethammer, S. Haker, and C. F. Westin. Geodesic-loxodromes for diffusion tensor interpolation and difference measurement. In *Med Image Comput Comput Assist Interv (MICCAI) 2007*, volume 4791 of *LNCS*, pages 1–9. Springer Berlin Heidelberg, 2007b. 3, 18, 31, 41, 42, 79

P. B. Kingsley. Introduction to diffusion tensor imaging mathematics: Part II. Anisotropy, diffusion-weighting factors, and gradient encoding schemes. *Concepts Magn Reson A*, 28:123–154, 2006. 74

P. B. Kingsley and W. G. Monahan. Contrast-to-noise ratios of diffusion anisotropy indices. *Magn Reson Med*, 53(4):911–918, 2005. 3, 74, 75

S. Krishnamoorthi, M. Sarkar, and W. S. Klug. Numerical quadrature and operator splitting in finite element methods for cardiac electrophysiology. *Int J Numer Method Biomed Eng*, 29(11):1243–1266, 2013. 2

G. L. Kung, T. C. Nguyen, A. Itoh, S. Skare, N. B. Ingels, Jr, D. C. Miller, and D. B. Ennis. The presence of two local myocardial sheet populations confirmed by diffusion tensor MRI and histological validation. *J Magn Reson Imaging*, 34 (5):1080–1091, 2011. 1, 2, 30

G. L. Kung, A. M. Ajijola, R. Tung, V. Vaseghi, J. K. Gahm, W. Zhou, A. Mahajan, A. Garfinkel, K. Shivkumar, and D. B. Ennis. Microstructural remodling in the porcine infarct border zone measured by diffusion tensor and late gadolinium enhancement MRI. In *AHA Scientific Sessions*, 2012. 47, 80

C. Lenglet, M. Rousson, R. Deriche, and O. Faugeras. Statistics on the manifold of multivariate normal distributions: theory and application to diffusion tensor MRI processing. *J Math Imaging Vis*, 25(3):423–444, 2006. 3, 18

S. E. Maier, H. Gudbjartsson, S. Patz, L. Hsu, K. O. Lovblad, R. R. Edelman, S. Warach, and F. A. Jolesz. Line scan diffusion imaging: characterization in healthy subjects and stroke patients. *Am J Roentgenol*, 171:85–93, 1998. 57

N. G. Papadakis, D. Xing, G. C. Houston, J. M. Smith, M. I. Smith, M. F. James, A. A. Parsons, C. L. Huang, L. D. Hall, and T. A. Carpenter. A study of rotationally invariant and symmetric indices of diffusion anisotropy. *Magn Reson Imaging*, 17(6):881–892, 1999. 74

X. Pennec, P. Fillard, and N. Ayache. A Riemannian framework for tensor computing. *Int J Comp Vis (IJCV)*, 66:41–66, 2006. 3, 18, 30, 41

C. Pierpaoli and P. J. Basser. Toward a quantitative assessment of diffusion anisotropy. *Magn Reson Med*, 36(6):893–906, 1996. 3, 52, 53, 60

William H. Press. *Numerical recipes in C++ : the art of scientific computing*. Cambridge University Press, Cambridge, UK; New York, 2nd edition, 2002. 16

D. F. Scollan, A. Holmes, R. Winslow, and J. Forder. Histological validation of myocardial microstructure obtained from diffusion tensor magnetic resonance imaging. *Am J Physiol*, 275(6):H2308–H2318, 1998. 1, 2

K. Shoemake. Animating rotation with quaternion curves. *ACM SIGGRAPH computer graphics*, 19(3):245–254, 1985. 2

S. Skare, M. Hedehus, M. E. Moseley, and T. Q. Li. Condition number as a measure of noise performance of diffusion tensor data acquisition schemes with MRI. *J Magn Reson*, 147:340–352, 2000. 54

A. G. Sorensen, O. Wu, W. A. Copen, T. L. Davis, R. G. Gonzalez, W. J. Koroshetz, T. G. Reese, B. R. Rosen, V. J. Wedeen, and R. M. Weisskoff. Human acute cerebral ischemia: detection of changes in water diffusion anisotropy by using MR imaging. *Radiology*, 212(3):785–792, 1999. 74

C. H. Sotak. The role of diffusion tensor imaging in the evaluation of ischemic brain injury - a review. *NMR Biomed*, 15(7-8):561–569, 2002. 2, 14, 73

E. O. Stejskal and J. E. Tanner. Spin diffusion measurements: spin echoes in the presence of a timedependent field gradient. *J Chem Phys*, 42:288, 1965. 54

G. J. Strijkers, A. Bouts, W. M. Blankesteijn, T. H. Peeters, A. Vilanova, M. C. van Prooijen, H. M. Sanders, E. Heijman, and K. Nicolay. Diffusion tensor imaging of left ventricular remodeling in response to myocardial infarction in the mouse. *NMR Biomed*, 22:182–190, 2009. 80

G. Thomalla, V. Glauche, M. A. Koch, C. Beaulieu, C. Weiller, and J. Röther. Diffusion tensor imaging detects early Wallerian degeneration of the pyramidal tract after ischemic stroke. *Neuroimage*, 22(4):1767–1774, 2004. 2, 14, 73

W. Y. Tseng, T. G. Reese, R. M. Weisskoff, and V. J. Wedeen. Cardiac diffusion tensor MRI in vivo without strain correction. *Magn Reson Med*, 42(2):393–403, 1999. 30

Z. Wang and B. Vemuri. DTI segmentation using an information-theoretic tensor dissimilarity measure. *IEEE Trans Med Imaging*, 24(10):1267–1277, 2005. 41, 42

Y. Wu, L. J. Zhang, C. Zou, H. F. Tse, and E. X. Wu. Transmural heterogeneity of left ventricular myocardium remodeling in postinfarct porcine model revealed by MR diffusion tensor imaging. *J Magn Reson Imaging*, 34:43–49, 2011. 80

F. Yang, Y. M. Zhu, I. E. Magnin, J. H. Luo, P. Croisille, and P. B. Kingsley. Feature-based interpolation of diffusion tensor fields and application to human cardiac DT-MRI. *Med Image Anal*, 16(2):459–481, 2012. 19, 31

L. Zhan, N. Jahanshad, D. B. Ennis, Y. Jin, M. A. Bernstein, B. J. Borowski, C. R. Jack, A. W. Toga, A. D. Leow, and P. M. Thompson. Angular versus spatial resolution trade-offs for diffusion imaging under time constraints. *Hum. Brain Mapp.*, 34:2688–2706, 2013. 70

X. Zhu, Z. Ghahramani, and J. Lafferty. Semi-supervised learning using Gaussian fields and harmonic functions. In *Int Conf Mach Learn (ICML)*, pages 912–919, 2003. 44